PHYSICS OF FLUIDS **21**, 105105 (2009)

# Theoretical prediction of turbulent skin friction on geometrically complex surfaces

Yulia Peet[a] and Pierre Sagaut
*Institut Jean le Rond d'Alembert, Université Pierre et Marie Curie—Paris 6, 75252 Paris Cedex 05, France*

(Received 16 December 2008; accepted 1 September 2009; published online 28 October 2009)

This article can be considered as an extension of the paper of Fukagata *et al.* [Phys. Fluids **14**, L73 (2002)] which derived an analytical expression for the constituent contributions to skin friction in a turbulent channel, pipe, and plane boundary layer flows. In this paper, we extend the theoretical analysis of Fukagata *et al.* (formerly limited to canonical cases with two-dimensional mean flow) to a fully three-dimensional situation allowing complex wall shapes. We start our analysis by considering arbitrarily shaped surfaces and then formulate a restriction on a surface shape for which the current analysis is valid. A theoretical formula for skin friction coefficient is thus given for streamwise and spanwise homogeneous surfaces of any shape, as well as some more complex configurations, including spanwise-periodic wavy patterns. The theoretical analysis is validated using the results of large eddy simulations of a turbulent flow over straight and wavy riblets with triangular and knife-blade cross-sections. Decomposition of skin friction into different constituent contributions allows us to analyze the influence of different dynamical effects on a skin friction modification by riblet-covered surfaces. *© 2009 American Institute of Physics*.
[doi:10.1063/1.3241993]

## I. INTRODUCTION

Accurate estimation of skin friction coefficient is required for determining skin friction drag on a body moving relative to a fluid. The negative impact of skin friction drag on performance and efficiency of practical engineering devices is responsible for the past and present quest for skin friction drag reduction methods. As a result, a great deal of experimental and computational data has been generated over the past several decades concerning skin friction and the ways to reduce it, and a number of various skin friction reduction methods have been proposed.[1]

It is now understood that turbulent flows have higher skin friction than their laminar counterparts due to the interaction of coherent near-wall turbulent structures or quasistreamwise vortices with the surface.[2] Quasistreamwise vortices pump a high-speed fluid toward the wall during the turbulent sweep events, thus increasing the local shear rate and, ultimately, the skin friction.[3] Reduction in this interaction would generally lead to a lower skin friction, and various passive and active skin friction reduction methods are attempting to alter the near-wall turbulence in one way or another in order to achieve this reduction. Wall blowing and suction, or opposition control of turbulence, prevents the downwash of high-speed fluid toward the wall during sweep events;[4,5] riblets[6,7] and microbubbles[8] displace the quasistreamwise vortices away from the wall, so that the vortex-surface interaction is reduced; spanwise-wall oscillation[9,10] breaks the coherence between the streamwise vortices and the low-speed streaks, thus weakening the near-wall burst activity and reducing skin friction.

However, in spite of the extensive literature on skin friction drag reduction, most of the conclusions are drawn based on hypothetical arguments relating the measured/calculated skin friction coefficient to the observed flow features. A clear understanding of the contribution of different dynamical effects to skin friction, based on theoretical analysis, is lacking. Fukagata *et al.*[11] derived an analytical expression relating the local skin friction coefficient to the properties of the flow above the surface for canonical cases of plane turbulent channel flow, pipe flow, and flat plate boundary layer. They used their analysis to explain skin friction modification by opposition control and uniform wall blowing/suction. Their approach was subsequently applied to analyze skin friction reduction by near-wall turbulence manipulation at high Reynolds numbers[12] and by superhydrophobic surfaces.[13] In addition, this analysis was recently extended to include compressible effects on skin friction in turbulent channel flow, pipe flow, and flat plate boundary layer at supersonic Mach numbers.[14]

Recently, Sbragaglia and Sugiyama[15] proposed an analytical expression for a skin friction drag on a surface as a function of the volume integral of the velocity field without assuming any particular shape of the surface or flow homogeneity. They used the derived expression to analyze drag modification of the flow in a plane channel with mixed-slip boundary conditions at small Reynolds numbers [$\mathrm{Re}\sim\mathcal{O}(1)$], as compared to the creeping flow solution. Although the relation proposed in Ref. 15 can be applied to three-dimensional geometries, it is given in a very general form, without spelling out specific expressions for different dynamical contributions, which is done in Refs. 11 and 14, but only for quasi-two-dimensional cases.

In the present paper, we extend the theoretical analysis of Fukagata *et al.*[11] (formerly limited to canonical cases with

---

[a] Electronic mail: peet@lmm.jussieu.fr.

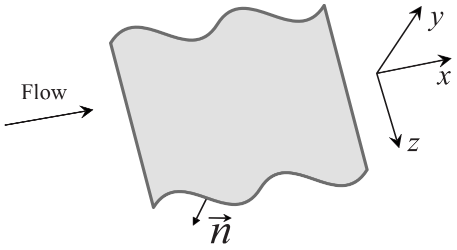

FIG. 1. Schematics of a flow over an arbitrarily shaped surface.

two-dimensional mean flow) to a fully three-dimensional case of complex wall shapes, giving exact closed-form expressions for different dynamical contributions into a skin friction (bulk, asymmetric, turbulent, etc.). The proposed generalization allows us to treat analytically laminar and turbulent flows in configurations involving geometrical surface modification, as it occurs with the use of riblets[6,7] or wall deforming actuators in active flow control.[5,16] It should be noted that unlike in Refs. 11 and 15, we confine our attention to the flows with zero wall velocity. Although this condition can be relaxed to account for effects of wall transpiration or slip, this is not the subject of the present paper.

In Sec. II, we present the details of the derivation of the closed-form expression relating the skin friction coefficient to the statistical information of the flow in a case of three-dimensional wall shapes. We start our analysis by considering arbitrarily shaped surfaces and then formulate a restriction on the surface shape for which the current analysis is valid. In Sec. III, we use the derived expression to analyze the modification of skin friction by straight[6,7] and wavy[17] riblets with two different types of cross-section: triangular and knife-blade. Statistical flow information needed for the analytical expression is obtained from large eddy simulations (LESs). The skin friction coefficient obtained from the analytical expression is compared to the directly computed value. The derived expression—allowing us to decompose skin friction coefficient into the sum of bulk, asymmetric, and turbulent components, provides better understanding of the mechanism of skin friction modification by straight and wavy riblets. In the present paper, we do not consider the pressure drag, which is nonzero for wavy riblets and needs to be included in the total drag estimation.[18]

## II. MATHEMATICAL FORMULATION

### A. Skin friction coefficient

Consider a flow over an arbitrarily shaped surface as depicted in Fig. 1. A Cartesian coordinate system $(x,y,z)$ is introduced, where $x$ axis is aligned with the direction of incoming flow, $y$ axis is parallel to the mean surface normal, and $z$ axis is in the spanwise direction.

The local force that acts on a surface at a particular point consists of shear and pressure forces

$$\vec{F} = -[\mu(\nabla\otimes\vec{v} + (\nabla\otimes\vec{v})^T)|_w\vec{n} - P_w\vec{n}], \tag{1}$$

where $\mu$ is the fluid viscosity, $\vec{v}=(u,v,w)$ is the velocity vector, $P$ is the pressure, $\vec{n}$ is the outward pointing local surface normal of the unit length, and the subscript $w$ stands for the quantities evaluated at the wall. Dimensional variables will be denoted with the superscript $^*$ throughout the paper. However, since all the variables are dimensional in Sec. II A, we will skip the superscript $^*$ in this section for the sake of brevity. In this paper, we derive an analytical formulation for the skin friction only, and therefore we will only look at the shear force. Pressure drag is not considered in this paper. Local shear force is

$$\vec{F}_{\text{sh}} = -\mu(\nabla\otimes\vec{v} + (\nabla\otimes\vec{v})^T)|_w\vec{n}, \tag{2}$$

and $x$-component of $\vec{F}_{\text{sh}}$ defines local skin friction drag

$$F_d = -\mu(\nabla\otimes\vec{v} + (\nabla\otimes\vec{v})^T)|_w\vec{n}\cdot\vec{i}, \tag{3}$$

where $\vec{i}$ is the unit vector in $x$ direction. It can be shown (see Appendix A) that local skin friction drag can be expressed as

$$F_d = -\mu\left.\left(\frac{\partial u}{\partial n} + \frac{\partial v_n}{\partial x}\right)\right|_w, \tag{4}$$

where $u$ is the streamwise velocity component and $v_n$ is the velocity component in the direction of a local surface normal.

Let us consider the second contribution to $F_d$, $-\mu(\partial v_n/\partial x)|_w$ and show that it is identically zero. First, we show that the gradient of any velocity component at the wall is aligned with the local surface normal. Consider a local coordinate system with the basis $(\vec{\tau}_1,\vec{n},\vec{\tau}_2)$, where $\tau_1$ and $\tau_2$ axes are tangential to the surface, and $n$ axis is aligned with the local surface normal. In this coordinate system, the gradient is written as

$$\nabla v_i = \frac{\partial v_i}{\partial\tau_1}\vec{\tau}_1 + \frac{\partial v_i}{\partial n}\vec{n} + \frac{\partial v_i}{\partial\tau_2}\vec{\tau}_2, \tag{5}$$

where $v_i$ is any arbitrary velocity component. At the wall, $v_i|_w=0$ due to the no-slip conditions, and so do its tangential derivatives: $(\partial v_i/\partial\tau_1)|_w=0$ and $(\partial v_i/\partial\tau_2)|_w=0$. This leaves the gradient at the wall a

$$\nabla v_i|_w = \left.\frac{\partial v_i}{\partial n}\right|_w\vec{n}, \tag{6}$$

which is in the direction of the local surface normal. Since the gradient is invariant under orthogonal transformations, its value and direction will remain the same when expressed in the original $(x,y,z)$ coordinate system.

Second, we express $\partial v_n/\partial x$ through the velocity gradient $\nabla v_n$ as

$$\frac{\partial v_n}{\partial x} = \nabla v_n\cdot\vec{i}, \tag{7}$$

and using Eq. (6) we get that at the wall

$$\left.\frac{\partial v_n}{\partial x}\right|_w = \left.\frac{\partial v_n}{\partial n}\right|_w\vec{n}\cdot\vec{i}. \tag{8}$$

Finally, we go back to the local coordinate system $(\tau_1,n,\tau_2)$ and look at the continuity equation at the wall in this local coordinate system (which is also invariant under orthogonal transformations),

$$\left(\frac{\partial v_{\tau_1}}{\partial \tau_1}+\frac{\partial v_n}{\partial n}+\frac{\partial v_{\tau_2}}{\partial \tau_2}\right)\Big|_w=0. \tag{9}$$

As already noted before, derivatives of any velocity component in the tangential directions $\tau_1$ and $\tau_2$ are zero at the wall, and therefore the normal derivative of the normal velocity component is also zero at every point at the wall

$$\left.\frac{\partial v_n}{\partial n}\right|_w=0, \tag{10}$$

transforming Eq. (8) into

$$\left.\frac{\partial v_n}{\partial x}\right|_w=0 \tag{11}$$

and proving that the second contribution to the local skin friction drag is identically zero.

Thus, local skin friction drag can be written as

$$F_d=-\mu\left.\left(\frac{\partial u}{\partial n}\right)\right|_w, \tag{12}$$

and its nondimensional counterpart, the skin friction coefficient defined as

$$C_f=\frac{F_d}{1/2\rho U_r^{*2}}, \tag{13}$$

is therefore expressed as

$$C_f=-\frac{2\mu}{\rho U_r^{*2}}\left.\left(\frac{\partial u}{\partial n}\right)\right|_w, \tag{14}$$

where $\rho$ is the density and $U_r^*$ is the reference velocity.

### B. Expression for the normal derivative

To derive an analytical expression for $C_f$ given by Eq. (14), one needs to estimate the normal derivative of streamwise velocity at the wall $(\partial u/\partial n)_w$. To do that in a general case of a turbulent flow, we start by evoking the Reynolds-averaged nondimensionalized momentum equation in the streamwise direction for an incompressible flow,

$$\frac{\partial \bar{u}}{\partial t}+\frac{\partial(\bar{u}\bar{u})}{\partial x}+\frac{\partial(\bar{u}\bar{v})}{\partial y}+\frac{\partial(\bar{u}\bar{w})}{\partial z}=-\frac{\partial \bar{P}}{\partial x}+\frac{1}{\mathrm{Re}}\left(\frac{\partial^2\bar{u}}{\partial x^2}+\frac{\partial^2\bar{u}}{\partial y^2}+\frac{\partial^2\bar{u}}{\partial z^2}\right)-\frac{\partial(\overline{u'u'})}{\partial x}-\frac{\partial(\overline{u'v'})}{\partial y}-\frac{\partial(\overline{u'w'})}{\partial z}. \tag{15}$$

A bar over variables denotes mean quantities, and a prime—the fluctuating components. Averages are defined as ensemble means; they are, in general, time dependent. Velocities are normalized by the characteristic velocity $U^*$, spatial coordinates are normalized by the characteristic length $L^*$, $\mathrm{Re}=U^*L^*/\nu^*$ is the Reynolds number of the flow, and $\nu^*$ is the kinematic viscosity. Throughout the rest of the paper, superscript $^*$ denotes dimensional variables, and variables without $^*$ are nondimensional ones. Note that with the above normalization and averaging Eq. (14) for skin friction coefficient will read

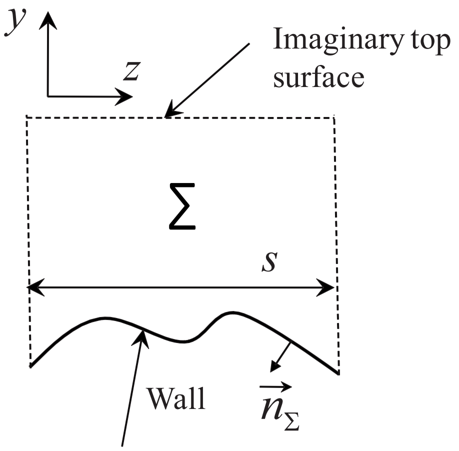

FIG. 2. Schematics of a cross-section $\Sigma$ at a streamwise location $x$.

$$\overline{C_f}=-\frac{2}{\mathrm{Re}U_r^2}\left.\left(\frac{\partial\bar{u}}{\partial n}\right)\right|_w, \tag{16}$$

where $U_r$ is nondimensional reference velocity $U_r=U_r^*/U^*$. Nondimensional reference velocity $U_r$ accounts for the possible difference between representative velocity $U_r^*$ in the definition of $C_f$ [Eqs. (13) and (14)] and characteristic velocity $U^*$ used for nondimensionalization of governing equations. Rearranging some terms, we rewrite Eq. (15) as

$$\bar{I}_t+\bar{I}_v=-\left(\bar{I}_x+\frac{\partial\bar{P}}{\partial x}+\frac{\partial\bar{u}}{\partial t}\right), \tag{17}$$

where $\bar{I}_x$ is the sum of the convective terms and streamwise turbulent and viscous stresses

$$\bar{I}_x=\frac{\partial(\bar{u}\bar{u})}{\partial x}+\frac{\partial(\bar{u}\bar{v})}{\partial y}+\frac{\partial(\bar{u}\bar{w})}{\partial z}+\frac{\partial(\overline{u'u'})}{\partial x}-\frac{1}{\mathrm{Re}}\frac{\partial^2\bar{u}}{\partial x^2}, \tag{18}$$

and $\bar{I}_t$, $\bar{I}_v$ are the crossflow turbulent and viscous terms, respectively,

$$\bar{I}_t=\frac{\partial(\overline{u'v'})}{\partial y}+\frac{\partial(\overline{u'w'})}{\partial z}, \tag{19}$$

$$\bar{I}_v=-\frac{1}{\mathrm{Re}}\left(\frac{\partial^2\bar{u}}{\partial y^2}+\frac{\partial^2\bar{u}}{\partial z^2}\right). \tag{20}$$

To proceed, we integrate Eq. (17) at each streamwise location $x$ over the cross-section $\Sigma$ shown in Fig. 2. Cross-section $\Sigma$ is the $y$-$z$ cross-section of the flow volume at a given streamwise location and represents the area occupied by the flow between the wall and an imaginary flat surface, which is perpendicular to the vertical axis and located far enough from the wall so that the flow at that location can be considered uniform. Such an imaginary surface would, for example, correspond to the edge of a boundary layer or to a channel center plane. Side boundaries of the cross-section $\Sigma$ are chosen to be parallel to the $y$ axis. The lateral spacing between the side boundaries is denoted by $s$. Please note that in the general case both $\Sigma$ and $s$ are functions of the streamwise coordinate $x$. Integrating Eq. (17) over $\Sigma$ gives

$$\int_{\Sigma}\int(\overline{I_t}+\overline{I_v})dydz=-\int_{\Sigma}\int\left(\overline{I_x}+\frac{\partial\bar{P}}{\partial x}+\frac{\partial\bar{u}}{\partial t}\right)dydz. \tag{21}$$

Using the Gauss–Ostrogradski theorem for the left-hand side of Eq. (21), we obtain

$$\int_{\Sigma}\int\overline{I_t}dydz=\oint_{\partial\Sigma}(\overline{u'v'}\vec{j}+\overline{u'w'}\vec{k})\cdot\vec{n}_{\Sigma}d\gamma=\oint_{\partial\Sigma}\overline{u'v'_{n_{\Sigma}}}d\gamma, \tag{22}$$

$$\begin{aligned}\int_{\Sigma}\int\overline{I_v}dydz&=-\frac{1}{\mathrm{Re}}\oint_{\partial\Sigma}\left(\frac{\partial\bar{u}}{\partial y}\vec{j}+\frac{\partial\bar{u}}{\partial z}\vec{k}\right)\cdot\vec{n}_{\Sigma}d\gamma\\&=-\frac{1}{\mathrm{Re}}\oint_{\partial\Sigma}\frac{\partial\bar{u}}{\partial n_{\Sigma}}d\gamma.\end{aligned} \tag{23}$$

In Eqs. (22) and (23), $\partial\Sigma$ is the contour of the cross-sectional area $\Sigma$, $\vec{n}_{\Sigma}$ is the in-plane outward pointing unit normal of the contour $\partial\Sigma$, and $\vec{j}$ and $\vec{k}$ are the unit vectors in $y$ and $z$ directions, respectively. Throughout this paper $\gamma$ denotes the local variable along the contour of integration, i.e., the length of the contour in Cartesian system from the start of integration to the local point and $d\gamma$ denotes the differential of the contour length. Notice that the contour $\partial\Sigma$ consists of three segments: a wall segment, a top segment corresponding to imaginary flat surface, and side segments. To proceed further, we formulate the boundary conditions on these three segments.

(1) Wall segment

No slip: $$\bar{u}=\bar{v}=\bar{w}=0,\qquad u'=v'=w'=0. \tag{24}$$

(2) Top segment

Uniform flow: $$\partial\bar{u}/\partial y=0,\qquad u'=v'=w'=0. \tag{25}$$

(3) Side segments

Periodicity: $$(\partial\bar{u}/\partial z)_l=(\partial\bar{u}/\partial z)_r,\qquad u'_l=u'_r,\quad v'_l=v'_r,\quad w'_l=w'_r. \tag{26}$$

For the wall and the top segments, specified boundary conditions hold for any surface (due to viscosity effects and particular choice of a top boundary). For the side segments, we assume periodicity conditions that are valid when a surface consists of a spanwise-periodic array of identical fragments resulting in the same flow properties on the fragment side boundaries (subscripts $l$ and $r$ refer to the left and right boundaries, respectively). Note that uniform flow conditions and symmetry conditions at side boundaries, both characterized by

$$\partial\bar{u}/\partial z=0,\quad u'=v'=w'=0, \tag{27}$$

are particular cases of periodicity conditions. Uniform flow conditions at side boundaries are valid if the wall shape approaches that of a flat plate at its spanwise ends, so that there are no end effects. Symmetry conditions at side boundaries are valid if the cross-sectional shape of the wall is symmetric and there are no other conditions violating the flow symmetry (such as nonzero spanwise velocity at the side segments, etc.). It can be easily seen that with the above boundary conditions the contour integral in the right-hand side of Eq. (22) is identically zero at all three segments (for the side boundaries with periodicity conditions the left and right integrals cancel each other),

$$\oint_{\partial\Sigma}\overline{u'v'_{n_{\Sigma}}}d\gamma=0. \tag{28}$$

The contour integral in the right-hand side of Eq. (23) is zero everywhere except at the wall segment $\partial\Sigma_w$,

$$\oint_{\partial\Sigma}\frac{\partial\bar{u}}{\partial n_{\Sigma}}d\gamma=\oint_{\partial\Sigma_w}\frac{\partial\bar{u}}{\partial n_{\Sigma}}d\gamma. \tag{29}$$

Therefore, combining Eqs. (21)–(29), we can express the integral of the normal derivative of streamwise velocity $\partial\bar{u}/\partial n_{\Sigma}$ over the wall segment $\partial\Sigma_w$ as

$$-\frac{1}{\mathrm{Re}}\int_{\partial\Sigma_w}\frac{\partial\bar{u}}{\partial n_{\Sigma}}d\gamma=-\int_{\Sigma}\int\left(\overline{I_x}+\frac{\partial\bar{P}}{\partial x}+\frac{\partial\bar{u}}{\partial t}\right)dydz. \tag{30}$$

Equation (30) is almost what we need to compute the skin friction coefficient from Eq. (16), except for the following mismatch. Derivative $\partial\bar{u}/\partial n_{\Sigma}$ in Eq. (30) is with respect to $\vec{n}_{\Sigma}$, which is the in-plane normal to the contour $\partial\Sigma$ at a given point. However, derivative $\partial\bar{u}/\partial n$ in Eq. (16) is with respect to $\vec{n}$, which is the normal to the original three-dimensional surface at the same point. Contour $\partial\Sigma$ lies in the $y$-$z$ plane, and so does $\vec{n}_{\Sigma}$ (see Fig. 2). However, surface normal $\vec{n}$ might not be oriented in the $y$-$z$ plane. In other words, we can view $\vec{n}_{\Sigma}$ as the orthogonal projection of $\vec{n}$ onto $y$-$z$ plane (with its magnitude adjusted to correspond to the unit length). We can relate $\partial\bar{u}/\partial n_{\Sigma}$ to $\partial\bar{u}/\partial n$ at the wall using the fact that the gradient of any velocity component at the wall is aligned with the local surface normal [Eq. (6)] and the fact that

$$\frac{\partial\bar{u}}{\partial n_{\Sigma}}=\nabla\bar{u}\cdot\vec{n}_{\Sigma}. \tag{31}$$

We can write that at the wall

$$\left.\frac{\partial\bar{u}}{\partial n_{\Sigma}}\right|_w=\left.\frac{\partial\bar{u}}{\partial n}\right|_w\vec{n}\cdot\vec{n}_{\Sigma}=\left.\frac{\partial\bar{u}}{\partial n}\right|_w\cos\beta, \tag{32}$$

where $\beta$ is the angle between the surface normal $\vec{n}$ and its orthogonal projection onto the $y$-$z$ plane, $\vec{n}_{\Sigma}$. Substituting Eq. (32) into Eq. (30) gives

$$-\frac{1}{\mathrm{Re}}\int_{\partial\Sigma_w}\frac{\partial\bar{u}}{\partial n}\cos\beta(\gamma)d\gamma=-\int_{\Sigma}\int\left(\bar{I}_x+\frac{\partial\bar{P}}{\partial x}+\frac{\partial\bar{u}}{\partial t}\right)dydz. \tag{33}$$

### C. Allowable surfaces

Since $\cos\beta$ is a function of the contour variable $\gamma$ in the general case, it is not possible to obtain an uncoupled expression for $\partial\bar{u}/\partial n$ in the general case. Therefore, in what follows we will only consider surfaces for which $\cos\beta$ is not a function of $\gamma$, but constant along $\partial\Sigma_w$ for every cross-section $\Sigma$. We will give some examples of surfaces which satisfy this requirement.

*Class 1:* Streamwise-homogeneous surfaces: surfaces whose shape does not depend on $x$ and which can be parametrized by a function $F(y,z)=0$. In this case, $\vec{n}$ and its $y$-$z$ projection $\vec{n}_\Sigma$ will be identical, $\beta=0$ and $\cos\beta=1$.

*Class 2:* Spanwise-homogeneous surfaces: surfaces whose shape does not depend on $z$ and which can be parametrized by a function $F(x,y)=0$. Then $\vec{n}$ will not be identical to $\vec{n}_\Sigma$. But an angle $\beta$ between $\vec{n}$ and $\vec{n}_\Sigma$ will not depend on $z$ and, since the $y$-coordinates of the points on a wall segment $\partial\Sigma_w$ will not depend on $z$ either, the angle $\beta$ will be the same for every $y$ and $z$ at a corresponding point on a wall segment $\partial\Sigma_w$; therefore, $\cos\beta$ will be constant along any wall segment $\partial\Sigma_w$.

*Class 3:* Quasistreamwise-homogeneous surfaces: if a streamwise-homogeneous surface is modified in a way such that any arbitrary $y$-$z$ cross-section is translated along the $z$ axis by any arbitrary distance, then angle $\beta$ will be the same along the wall segment $\partial\Sigma_w$ for a given $x$, since every infinitesimal surface element is rotated by the same angle from its original location for a given $x$. Surfaces modified in this way still possess nonvarying $y$-$z$ cross-sectional shape, but they are not strictly streamwise homogeneous, since dependence on $x$ now exists.

Besides the surfaces described above, there can be other surfaces which satisfy the requirement $\cos\beta=\text{const}$ along each $\partial\Sigma_w$. Generally, if we have a surface defined by a function $F(x,y,z)=0$, then a surface normal at a point $(x,y,z)$ is given by the gradient of $F$, $\vec{n}=(F_x,F_y,F_z)$, and its projection to the $y$-$z$ plane by a vector $\vec{n}_\Sigma=(0,F_y,F_z)$. Note that in this formulation $\vec{n}$ and $\vec{n}_\Sigma$ do not necessarily have unit length. The cosine of the angle between the two vectors is given by

$$\cos\beta=\frac{\vec{n}\cdot\vec{n}_\Sigma}{|\vec{n}||\vec{n}_\Sigma|}=\sqrt{\frac{F_y^2+F_z^2}{F_x^2+F_y^2+F_z^2}}, \tag{34}$$

and, therefore, surfaces for which $\cos\beta$ is constant along $\partial\Sigma_w$ can be generally defined as surfaces for which the following condition holds:

$$\sqrt{\frac{F_y^2+F_z^2}{F_x^2+F_y^2+F_z^2}}=\text{const}\quad\text{for } x=\text{const}. \tag{35}$$

Note that except for the condition of constant $\cos\beta$ defined by Eq. (35), surfaces under consideration should also guarantee that the flow boundary conditions (26) are satisfied on side boundaries with the incoming flow parallel to the $x$ axis. If a particular surface is such that only Eq. (35) is satisfied, but not Eq. (26), a new surface should be constructed consisting of a spanwise-periodic array of the given surface fragments, so that periodicity flow conditions on side boundaries are valid.

### D. Spanwise-averaged coefficient

When $\cos\beta(\gamma)=\text{const}$ along $\partial\Sigma_w$, Eq. (33) can be rewritten as

$$-\cos\beta\frac{1}{\mathrm{Re}}\int_{\partial\Sigma_w}\frac{\partial\bar{u}}{\partial n}d\gamma=-\int_{\Sigma}\int\left(\bar{I}_x+\frac{\partial\bar{P}}{\partial x}+\frac{\partial\bar{u}}{\partial t}\right)dydz. \tag{36}$$

It follows from Eq. (16) that

$$-\frac{1}{\mathrm{Re}}\int_{\partial\Sigma_w}\frac{\partial\bar{u}}{\partial n}d\gamma=\frac{U_r^2}{2}s\overline{C_f}^z, \tag{37}$$

where $\overline{C_f}^z$ is the spanwise-averaged skin friction coefficient defined as

$$\overline{C_f}^z(x,t)=\frac{1}{s}\int_{\partial\Sigma_w}\overline{C_f}(x,z,t)d\gamma. \tag{38}$$

Therefore, Eq. (36) reads

$$\frac{U_r^2 s\cos\beta}{2}\overline{C_f}^z=-\int_{\Sigma}\int\left(\bar{I}_x+\frac{\partial\bar{P}}{\partial x}+\frac{\partial\bar{u}}{\partial t}\right)dydz. \tag{39}$$

Multiplication of Eq. (39) by $1/A_\Sigma$, where $A_\Sigma$ is the area of the cross-section $\Sigma$, its subsequent subtraction from Eq. (17) results in the following expression for a spanwise-averaged skin friction coefficient:

$$\overline{C_f}^z=\frac{2A_\Sigma}{U_r^2 s\cos\beta}(\bar{I}_t+\bar{I}_v+F''), \tag{40}$$

where

$$F''=I_x''+\frac{\partial P''}{\partial x}+\frac{\partial u''}{\partial t} \tag{41}$$

and

$$f''(x,y,z,t)=\bar{f}(x,y,z,t)-\frac{1}{A_\Sigma}\int_{\Sigma}\int\bar{f}(x,y,z,t)dydz. \tag{42}$$

### E. Constituent contributions

To obtain the relation for the constituent contributions of different dynamical effects to the skin friction coefficient, Fukagata *et al.*[11] in their analysis of a homogeneous case of a plane channel flow applied triple integration of the form $\int_0^1 dy\int_0^y dy\int_0^y dy$ to the expression for the skin friction coefficient corresponding to Eq. (40) in our case ($y=0$ and $y=1$ signified the bottom wall and the channel center plane, respectively, in their normalization). With the three-dimensional shape of the wall, the situation is a little bit more complicated, and a line integration $\int dy$ should be replaced by a surface integration $\int\int dydz$ over elementary sur-

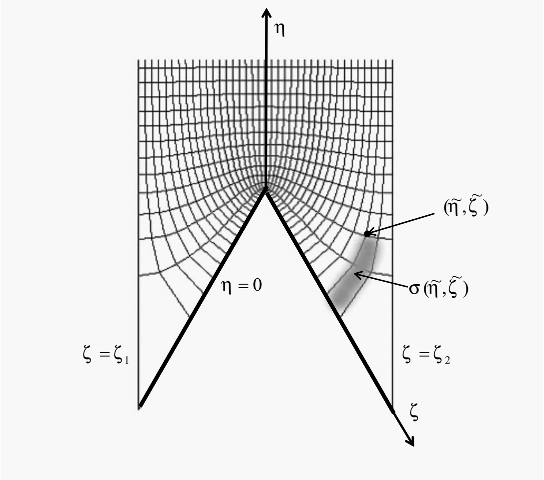

FIG. 3. Schematic of an orthogonal body-fitted curvilinear coordinate system $(\eta,\zeta)$.

faces within $\Sigma$. To ensure orthogonality, an integration has to be performed along the gridlines corresponding to the orthogonal body-fitted curvilinear coordinate system $(\eta,\zeta)$. Notice that we do not switch coordinate systems, Navier–Stokes equations are not modified, all distances are calculated in the Cartesian coordinate system, and functions $\eta(y,z),\zeta(y,z)$ are merely used to define elementary surfaces of integration. A schematic of an orthogonal body-fitted curvilinear coordinate system is shown in Fig. 3. Note that the wall is represented by $\eta=0$, the top surface by $\eta=\eta^{\text{top}}$, and the side boundaries by $\zeta=\zeta_1$ and $\zeta=\zeta_2$, respectively.

To proceed with our analysis, we integrate Eq. (40) over elementary surfaces $\sigma(\eta,\zeta)$, which, at every streamwise location $x$, are defined as (see Fig. 3)

$$\sigma(\eta,\zeta)=\{(y,z):\eta(y,z)\in(0,\eta),\zeta(y,z)\in(\zeta,\zeta+d\zeta)\}. \tag{43}$$

To integrate Eq. (40) over $\sigma(\eta,\zeta)$, we write

$$\int_\sigma\int\overline{C_f^z}dydz=\frac{2A_\Sigma}{U_r^2 s\cos\beta}\left[\int_\sigma\int(\overline{I_t}+\overline{I_v})dydz+\int_\sigma\int F''dydz\right]. \tag{44}$$

The left-hand side of Eq. (44) can be reduced to

$$\int_\sigma\int\overline{C_f^z}dydz=\overline{C_f^z}dA_\sigma, \tag{45}$$

where $dA_\sigma$ is the area of an elementary surface $\sigma$. For the first term in the right-hand side of Eq. (44), we can again use the Gauss–Ostrogradski theorem and transform

$$\int_\sigma\int(\overline{I_t}+\overline{I_v})dydz=\oint_{\partial\sigma}\overline{u'v'_{n_\sigma}}d\gamma-\frac{1}{\text{Re}}\oint_{\partial\sigma}\frac{\partial\overline{u}}{\partial n_\sigma}d\gamma. \tag{46}$$

To extract the skin friction coefficient out of Eq. (46), we write the contour integral in the last term in that equation as the sum of integrals over the wall segment $\partial\sigma_w$, top segment $\partial\sigma_t$, and side segments $\partial\sigma_s$ of the integration contour $\partial\sigma$,

$$-\frac{1}{\text{Re}}\oint_{\partial\sigma}\frac{\partial\overline{u}}{\partial n_\sigma}d\gamma=-\frac{1}{\text{Re}}\left[\int_{\partial\sigma_w}\frac{\partial\overline{u}}{\partial n_\sigma}d\gamma+\int_{\partial\sigma_t}\frac{\partial\overline{u}}{\partial n_\sigma}d\gamma+\int_{\partial\sigma_s}\frac{\partial\overline{u}}{\partial n_\sigma}d\gamma\right]. \tag{47}$$

Following Eqs. (16) and (32) and using the fact that we are considering the surfaces where $\cos\beta=\text{const}$ along $\partial\Sigma_w$, the integral of $\partial\overline{u}/\partial n_\sigma$ over the wall segment $\partial\sigma_w$ can be related to the skin friction coefficient as follows. Let us introduce the weight function $w(\gamma)$ as the ratio of the local skin friction coefficient $\overline{C_f}(\gamma)$ at a location $\gamma$ along the wall segment $\partial\Sigma_w$ to the spanwise-averaged skin friction coefficient $\overline{C_f^z}$ at a given streamwise coordinate $x$ and a given time $t$,

$$w(\gamma)=\frac{\overline{C_f}(\gamma)}{\overline{C_f^z}}. \tag{48}$$

Then the first term in the right-hand side of Eq. (47) can be written as

$$\begin{aligned}-\frac{1}{\text{Re}}\int_{\partial\sigma_w}\frac{\partial\overline{u}}{\partial n_\sigma}d\gamma&=-\cos\beta\frac{1}{\text{Re}}\int_{\partial\sigma_w}\frac{\partial\overline{u}}{\partial n}d\gamma\\&=\frac{U_r^2\cos\beta}{2}\int_{\partial\sigma_w}\overline{C_f}(\gamma)d\gamma\\&=\frac{U_r^2\cos\beta}{2}\overline{C_f^z}\int_{\partial\sigma_w}w(\gamma)d\gamma\end{aligned} \tag{49}$$

With the use of Eqs. (46), (47), and (49), the integration over an elementary area $\sigma$, defined by Eq. (44), results in the following relation:

$$\overline{C_f^z}\int_{\partial\sigma_w}\left(w(\gamma)\frac{d\gamma}{s}-\frac{dA_\sigma}{A_\Sigma}\right)=\frac{1}{U_r^2 s\cos\beta}\left[\frac{2}{\text{Re}}\int_{\partial\sigma_s+\partial\sigma_t}\frac{\partial\overline{u}}{\partial n_\sigma}d\gamma+\int_\sigma\int(-2F'')dydz+\int_{\partial\sigma_s+\partial\sigma_t}(-2\overline{u'v'_{n_\sigma}})d\gamma\right]. \tag{50}$$

The fact that $u'=v'=w'=0$ at the wall was used to transform an integral $\oint_{\partial\sigma}\overline{u'v'_{n_\sigma}}d\gamma$ into an integral $\int_{\partial\sigma_s+\partial\sigma_t}\overline{u'v'_{n_\sigma}}d\gamma$ in Eq. (50).

The next step is to apply double integration of the form $\int_0^{\eta^{\text{top}}}d\gamma\int_0^{\eta}d\gamma$ to Eq. (50). Finally, we let $d\zeta$ in the definition of elementary surfaces $\sigma$, Eq. (43), be infinitesimally small and sum over all $d\zeta$. It is easy to see that the contributions from the side segments $\partial\sigma_s$ cancel each other during the summation. Transformation of all the terms of Eq. (50) under the procedure of double integration along $\eta$ and summation over $d\zeta$ is derived in Appendix B. As a result, one gets the following formula for the spanwise-averaged skin friction coefficient in a turbulent flow over any three-dimensional surface which satisfies Eqs. (26) and (35),

$$\overline{C_f}^z(x,t)=\frac{1}{U_r^2\mathcal{A}s\cos\beta}(T_b+\mathcal{T}_a+\mathcal{T}_p+\mathcal{T}_{\mathrm{tr}}+\mathcal{T}_t), \tag{51}$$

where $\mathcal{A}$, $\mathcal{T}_b$, $(\mathcal{T}_a+\mathcal{T}_p+\mathcal{T}_{\mathrm{tr}})$, and $\mathcal{T}_t$ are defined by Eqs. (B1)–(B4) of the Appendix B, respectively. $\mathcal{A}$ in the normalization term is a function of a cross-sectional shape and a spanwise skin friction distribution $w(\gamma)$. Note that all terms in Eq. (51) except for $U_r$ are functions of the streamwise coordinate $x$ in a general case. $\mathcal{T}_b$ corresponds to the bulk contribution, $\mathcal{T}_a$—the asymmetric contribution, $\mathcal{T}_p$—the pressure contribution, $\mathcal{T}_{\mathrm{tr}}$—the transient contribution, and $\mathcal{T}_t$—the turbulent contribution into the skin friction.

## III. APPLICATION OF THE FORMULA

In this section, we will show some examples of the application of the derived expression for the skin friction coefficient, Eq. (51), to realistic flows. This will serve a dual purpose of validating the formula and demonstrating its utility in extracting new information about the flow.

### A. Plane channel flow

A necessary step for validating any general-purpose formula is to check whether it reduces to its simpler counterpart in the limiting case. Fukagata *et al.*[11] provided an expression for a local skin friction coefficient as a function of statistical flow information for a plane turbulent channel flow. In this paragraph, we apply Eq. (51), derived for the case of geometrically complex surfaces, to a plane channel flow. We assume that the channel has a width $s$, its bottom wall is located at $y=0$, and its center plane corresponding to the top imaginary surface is located at $y=\delta$. Since the plane surface is a streamwise-homogeneous surface, $\beta=0$ and $\cos\beta=1$. Then Eq. (51) reduces to

$$\begin{aligned}\overline{C_f}^z(x,t)&=\overline{C_f}(x,z,t)\\&=\frac{3}{U_r^2\delta^2}\Bigg[\frac{2U_b\delta}{\mathrm{Re}}+\int_0^\delta(\delta-y)^2(-I''_x)dy\\&\quad+\int_0^\delta(\delta-y)^2\left(-\frac{\partial P''}{\partial x}\right)dy+\int_0^\delta(\delta-y)^2\\&\quad\times\left(-\frac{\partial u''}{\partial t}\right)dy+\int_0^\delta(\delta-y)(-2\overline{u'v'})dy\Bigg].\end{aligned} \tag{52}$$

We used the fact that $A_\Sigma=\delta s$ and the flow is homogeneous in the spanwise direction, giving $\overline{C_f}(\gamma)=\overline{C_f}^z$, $w(\gamma)=1$, and, therefore,

$$\mathcal{A}=\int_{-s/2}^{s/2}\int_0^\delta(\delta-y)\frac{1}{s}\left(1-\frac{y}{\delta}\right)dydz=\frac{\delta^2}{3}. \tag{53}$$

Equation (52) coincides exactly with Eq. (11) of Fukagata *et al.*[11] derived for the plane channel flow, if one substitutes $\delta=1$, $U_r=U_b=1/2$, $\mathrm{Re}=\mathrm{Re}_b$, corresponding to the normalization used in Ref. 11. However, notice the difference in notation concerning the constituent contributions into the skin friction with Ref. 11. What Fukagata *et al.*[11] call the "laminar term" [the first term in Eqs. (51) and (52)] is called the "bulk term" in the present paper, and what they call the "inhomogeneous term" [the second term in Eqs. (51) and (52)], we call the "asymmetric term." The reasons for the change in notation are the following. If we look at the skin friction coefficient in a laminar flow, then for a steady plane channel flow it will be equal to the first term in Eqs. (51) and (52), since all other terms will be identically zero. This fact probably made Fukagata *et al.*[11] call the first term in Eqs. (51) and (52) the laminar term. However, for a laminar flow over nonhomogeneous surfaces, the second term will not necessarily be zero (which will be shown later in this paper). So, the first term will not be the only contribution into the laminar skin friction for nonhomogeneous surfaces. That is why we thought that it would be misleading to call the first term in Eqs. (51) and (52) the laminar term and change the terminology as compared to Ref. 11. The second term in Eqs. (51) and (52) (called inhomogeneous term by Fukagata *et al.*[11]) was also renamed to the asymmetric term, since inhomogeneity contributes to all the terms in Eq. (51) in a geometrically complex case, and not just to the second term, through streamwise-dependent functions $\mathcal{A}$, $s$, and $\cos\beta$ in the denominator. The name "asymmetric" reflects the fact that this term is identically zero if the flow at the corresponding spanwise cross-section is symmetric with respect to the cross-sectional axis of symmetry, and is nonzero if the flow is asymmetric, as discussed below in more details.

### B. Surface riblets

#### *1. Geometry definition*

Riblet-covered surfaces are used because they exhibit lower skin friction drag in a turbulent flow than a flat surface. A three-dimensional as well as transverse view of a riblet-covered surface underneath a flat surface is shown in Fig. 4. In the present paper, we look at riblets with triangular and knife-blade cross-sections. Both types of riblet cross-section together with some basic parameters defining the cross-sectional geometry are shown in Fig. 5. The orthogonal body-fitted curvilinear coordinate system $(\eta,\zeta)$ utilized for performing integrations in Eqs. (B1)–(B4) is also shown for reference. For both triangular and knife-blade riblets, analytical formulas for the transformation from a Cartesian coordinate system $(y,z)$ into a curvilinear orthogonal system $(\eta,\zeta)$ are provided by Bechert and Bartenwerfer[19] and represent a series of conformal mappings from a surface inside a rectangular channel onto a surface inside a polygon. For triangular riblets, $y=0$ corresponds to the midpoint between a valley and a tip, and for knife-blade riblets it corresponds to the bottom part of the riblet surface, so that the cross-sectional area $A_\Sigma=\delta s$ for both types of cross-section.

We investigate both straight and wavy riblets. Straight riblets represent straight lines if viewed from above, while wavy riblets represent sinusoidal waves, see Fig. 6, characterized by the function

$$\Delta z(x)=a\sin\left(\frac{2\pi}{\lambda}x\right), \tag{54}$$

where $\Delta z(x)$ is the deviation of the spanwise coordinate of the wavy riblet surface from the corresponding spanwise coordinate of the straight riblet surface, $a$ is the oscillation

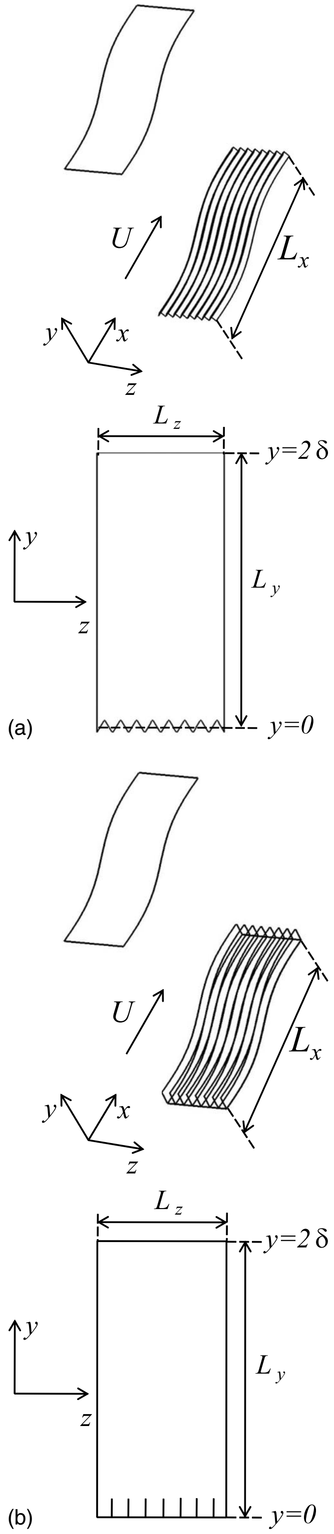

FIG. 4. Riblet geometry. Three-dimensional and transverse view. (a) Triangular riblets. (b) Knife-blade riblets.

amplitude, and λ is the oscillation wavelength. Note that the dependence of cross-sectional geometry on the streamwise coordinate is absent for both straight and wavy riblets.

Straight riblets belong to the Class 1 surfaces (streamwise-homogeneous surfaces) in the classification of Sec. II C. Triangular wavy riblets belong to the Class 3 surfaces in this classification (quasistreamwise-homogeneous surfaces). Note that in this case the angle $\beta(x)$ defined as

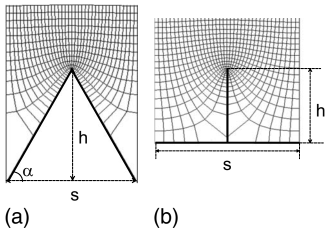

FIG. 5. Cross-sectional shape of riblets. Orthogonal body-fitted curvilinear coordinate system $(\eta,\zeta)$ is also shown. (a) Triangular cross-section. (b) Knife-blade cross-section.

$$\beta(x) = \arctan\left(\frac{d\Delta z}{dx}\right) \tag{55}$$

(see Fig. 6) is the same angle which enters Eq. (51) for the skin friction coefficient and represents the angle between the local surface normal and its orthogonal projection onto the $y$-$z$ plane. For knife-blade riblets, however, the situation is slightly different, since the riblet surface contains segments which are flat planes perpendicular to the $y$ axis. When a spanwise oscillation is introduced to the knife-blade riblet surface, the side segments become tilted with respect to the $x$ direction, so that the angle between the local surface normal $\vec{n}$ and its $y$-$z$ projection $\vec{n}_\Sigma$ becomes equal to $\beta$, as in the case of wavy riblets with other cross-sections (triangular, scalloped, etc.). However, for the bottom segments (which are flat planes perpendicular to the $y$ axis even after the spanwise oscillation is introduced) the local surface normal $\vec{n}$ is aligned with the $y$ axis and therefore with $\vec{n}_\Sigma$, resulting in $\beta=0$ for the bottom segments. Therefore, the condition of constant cos $\beta$ along the wall segment $\partial\Sigma_w$ of the $y$-$z$ cross-sections $\Sigma$ will generally not hold for wavy knife-blade riblets. However, in the present investigation we only consider small amplitudes in Eq. (54) resulting in small angles $\beta$ (below 9.6° for knife-blade riblets), so that the value of $(1/\cos\beta)$ does not exceed 1.015, and uncertainties coming from the condition of nonconstant $\beta$ are not expected to exceed 1.5%. Note that the assumption of Eq. (55), used throughout the rest of the paper, is exact for straight knife-blade riblets and for straight and wavy triangular riblets.

### *2. Parameter $\mathcal{A}$*

To estimate the parameter $\mathcal{A}$ entering the normalization term in Eq. (51), one needs to evaluate Eq. (B1) at a local cross-section $\Sigma$. There are two components which influence the value of $\mathcal{A}$: the shape of the cross-section and the span-

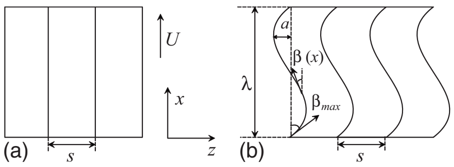

FIG. 6. Comparison between straight and wavy riblets. View of the riblet-covered surface from above. (a) Straight riblets. (b) Wavy riblets.

wise distribution of skin friction along the wall $w(\gamma)$. Cross-sectional shape is the geometrical parameter of the problem and is known *a priori*. However, the spanwise distribution of the skin friction coefficient ratio along the wall $w(\gamma) = \overline{C_f}(\gamma)/\overline{C_f}^z$ is generally unknown for the case of a turbulent flow over complex surfaces. In order to be able to predict the skin friction coefficient according to Eq. (51), in spite of the fact that we do not know the exact distribution of $w(\gamma)$ *a priori*, we approximate $w(\gamma)$ for a turbulent flow over straight or wavy riblets as the spanwise distribution of the skin friction coefficient ratio in a laminar flow over straight riblets with the same cross-section. As was shown by Bechert and Bartenwerfer,[19] for a viscous laminar flow over straight riblets without pressure gradient, the governing equations reduce to the Laplace equation for the streamwise velocity $u$,

$$\frac{\partial^2 u}{\partial y^2} + \frac{\partial^2 u}{\partial z^2} = 0. \tag{56}$$

The authors of Ref. 19 show that since arbitrary functions $f(z+\imath y)$ are solutions of the Laplace equation (56), distribution of the laminar velocity $u$ over a particular riblet surface can be obtained by mapping uniform Couette shear flow above a smooth plane surface onto that above the particular riblet surface. In other words, when the orthogonal curvilinear grid $(\eta,\zeta)$ depicted in Fig. 3 is constructed for a riblet surface by a conformal transformation from a Cartesian channel grid, the lines $\eta=$const represent the lines of constant velocity $u$, and the lines $\zeta=$const represent the force lines, i.e., the lines between which the constant shear force is transmitted, see Ref. 19. This means that the product $C_f(\gamma)d\gamma$ will be constant between each two neighboring $\zeta$ grid lines of an orthogonal curvilinear grid along $\partial\Sigma_w$. The beauty of this fact is that we can now find the spanwise distribution of the skin friction coefficient ratio $w(\gamma)$ in a laminar flow over straight riblets from the relation

$$C_f(\gamma)d\gamma = \text{const} = s\overline{C_f}^z \frac{d\zeta}{\zeta_2 - \zeta_1}, \tag{57}$$

from which it follows that

$$w(\gamma) = \frac{d\zeta}{\zeta_2 - \zeta_1}\frac{s}{d\gamma}. \tag{58}$$

This allows to simplify Eq. (B1) as

$$\mathcal{A} = \int_{\zeta_1}^{\zeta_2}\int_0^{\eta^{\text{top}}} [\gamma(\eta^{\text{top}}) - \gamma(\eta)]\left(\frac{d\zeta}{\zeta_2 - \zeta_1} - \frac{dA_\sigma}{A_\Sigma}\right) d\gamma(\eta), \tag{59}$$

and $\mathcal{A}$ becomes solely a function of the cross-sectional geometry. Note again that Eq. (59) for evaluating $\mathcal{A}$ is an exact consequence of a general equation (B1) for laminar streamwise-homogeneous flows while it is an approximation for turbulent flows and nonstreamwise-homogeneous flows. Nonetheless, since our intention for developing a theoretical expression for skin friction coefficient was to come up with the predictive formula, Eq. (59) is used for evaluating $\mathcal{A}$ throughout Sec. III B, and not the original Eq. (B1), since Eq. (B1) requires *a priori* knowledge of skin friction coefficient ratio and Eq. (59) does not.

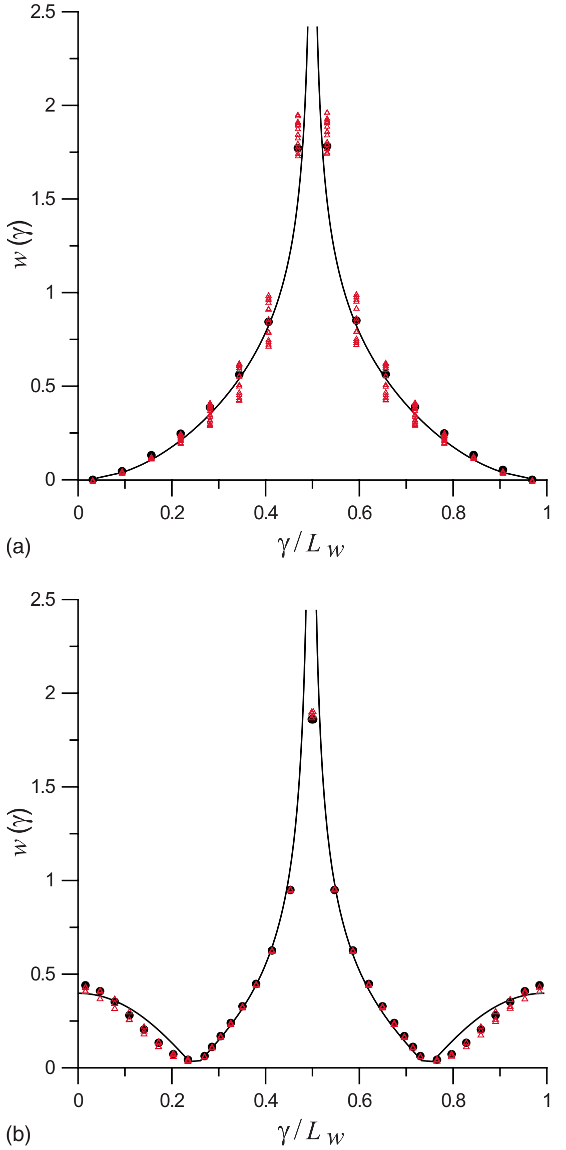

FIG. 7. (Color online) Spanwise distribution of skin friction coefficient ratio $w(\gamma)$. ——, Straight riblets laminar flow, Eq. (58); ●, straight riblets turbulent flow, LES ("straight T" and "straight B" cases in Table I); △, wavy riblets turbulent flow, LES ("short waves T" and "short waves B" cases in Table I). (a) Triangular riblets. (b) Knife-blade riblets.

Spanwise distribution of the skin friction coefficient ratio $w(\gamma)$ for straight and wavy riblets in a turbulent flow computed with LES method was compared *a posteriori* with the theoretical value of $w(\gamma)$ for straight riblets in a laminar flow given by Eq. (58) to estimate the extent of inaccuracy introduced by approximating $w(\gamma)$ in turbulent and nonhomogeneous flows by its laminar homogeneous counterpart for calculating $\mathcal{A}$. The results of this comparison are plotted in Fig. 7(a) for triangular riblets and in Fig. 7(b) for knife-blade riblets versus $\gamma/L_w$, where $L_w$ is the length of the wall segment $\partial\Sigma_w$. The exact geometry of the calculated cases is defined later in the paper (Table I). We see that for turbulent flow over straight riblets the spanwise distribution of the skin friction coefficient is very close to the laminar distribution

TABLE I. Geometrical parameters for the calculated cases.

| Case | $\alpha$ (deg) | $\beta_{\max}$ (deg) | $s/\delta$ | $h/s$ | $a/\delta$ | $\lambda/\delta$ | $s^+$ | $h^+$ | $a^+$ | $\lambda^+$ |
|---|---|---|---|---|---|---|---|---|---|---|
| Straight T | 60 | 0 | 0.1164 | 0.866 | 0 | 0 | 21 | 18 | 0 | 0 |
| Short waves T | 60 | 11.3 | 0.1164 | 0.866 | 0.1 | 3.22 | 21 | 18 | 18 | 580 |
| Long waves T | 60 | 11.3 | 0.1164 | 0.866 | 0.19 | 6 | 21 | 18 | 34 | 1080 |
| Straight B | 90 | 0 | 0.0908 | 0.5 | 0 | 0 | 16 | 8 | 0 | 0 |
| Short waves B | 90 | 9.6 | 0.0908 | 0.5 | 0.085 | 3.22 | 16 | 8 | 15 | 580 |
| Long waves B | 90 | 9.6 | 0.0908 | 0.5 | 0.16 | 6 | 16 | 8 | 28 | 1080 |

calculated from Eq. (58) both in triangular and knife-blade cases. For wavy surfaces the scatter is a bit higher, especially in the triangular case, due to a streamwise variation in the flow. Nonetheless, a streamwise-averaged value of $w(\gamma)$ is close to the theoretical laminar value of Eq. (58). Therefore, replacing the exact equation (B1) with Eq. (59) for evaluating $\mathcal{A}$ in order to achieve predictive capabiliity introduces only a very slight approximation. In both triangular and knife-blade cases, the maximum of $\overline{C_f}/\overline{C_f^z}$ occurs at the riblet tip ($\gamma/L_w=0.5$), and the minimum of $\overline{C_f}/\overline{C_f^z}$ occurs at the riblet valley ($\gamma/L_w=0,1$ for triangular riblets and $\gamma/L_w=0.25,0.75$ for knife-blade riblets).

### *3. Surface-averaged skin friction coefficient*

Since wavy riblet geometry exhibits periodicity in streamwise direction, we further integrate Eq. (51) in $x$ over the oscillation wavelength $\lambda$, which leads to

$$\overline{\overline{C}}_f=\frac{1}{U_r^2\mathcal{A}s\lambda}\left[\int_0^\lambda\frac{\mathcal{T}_b}{\cos\beta}dx+\int_0^\lambda\frac{\mathcal{T}_a}{\cos\beta}dx\right.$$
$$\left.+\int_0^\lambda\frac{\mathcal{T}_t}{\cos\beta}dx\right]=\overline{\overline{C}}_{fb}+\overline{\overline{C}}_{fa}+\overline{\overline{C}}_{ft}, \qquad (60)$$

where

$$\mathcal{T}_a=\int_{\zeta_1}^{\zeta_2}\int_0^{\eta^{\mathrm{top}}}[\gamma(\eta^{\mathrm{top}})-\gamma(\eta)]^2(-I''_{xr})d\gamma(\eta)d\gamma(\zeta), \qquad (61)$$

$$I''_{xr}=\frac{\partial(\overline{u}\overline{v})}{\partial y}+\frac{\partial(\overline{u}\overline{w})}{\partial z}-\frac{1}{A_\Sigma}\int_\Sigma\int\left(\frac{\partial(\overline{u}\overline{v})}{\partial y}+\frac{\partial(\overline{u}\overline{w})}{\partial z}\right)dydz, \qquad (62)$$

$\mathcal{T}_b$ and $\mathcal{T}_t$ are defined by Eqs. (B2) and (B4), as previously, $\overline{\overline{C}}_f$ represents a surface-averaged skin friction coefficient, and $\overline{\overline{C}}_{fb}$, $\overline{\overline{C}}_{fa}$, and $\overline{\overline{C}}_{ft}$ denote bulk, asymmetric, and turbulent contributions to the surface-averaged skin friction coefficient, respectively. To arrive at Eqs. (60)–(62), periodicity in $x$ direction was exploited leading to the disappearance of the terms containing streamwise derivatives $\partial/\partial x$ during integration over the period $\lambda$. Note that for the disappearance of the pressure term $\mathcal{T}_p$, we do not need to assume the absence of a mean flow pressure gradient, but only periodicity of its inhomogeneous part

$$P''=\overline{P}-\frac{1}{A_\Sigma}\int_\Sigma\int\overline{P}dydz \qquad (63)$$

[cf. Eqs. (B3) and (42)]. We also used an assumption of stationary mean flow leading to the disappearance of the transient term $\mathcal{T}_{\mathrm{tr}}$, and the independence of $x$ of $s$ and $\mathcal{A}$ [$\mathcal{A}$ is evaluated with Eq. (59)]. For straight riblets, we use the length of the computational domain in the streamwise direction $L_x$ as the period of integration $\lambda$.

To investigate the behavior of the skin friction coefficient in a turbulent flow over riblet surfaces using Eq. (60), large eddy simulations were performed for the case of straight and wavy riblets with triangular and knife-blade cross-sections. Simulations were set up in a channel, whose bottom wall was covered with riblets and the top wall was flat, please refer to Fig. 4 for the sketch of computational geometry. We use $U^*=U_b^*$ and $L^*=\delta^*$ for normalization, and we set Reynolds number $\mathrm{Re}=U_b^*\delta^*/\nu^*=2730$. Here $U_b^*$ is the bulk velocity and $\delta^*$ is the channel half-width defined in Fig. 4 (superscript $^*$ for dimensional variables is omitted in Fig. 4). Geometrical parameters for the calculated cases are listed in Table I and numerical grid parameters are listed in Table II. "T" stands for triangular and "B" for knife-blade riblets in these and subsequent tables. For the cross-sectional shape of the riblets we chose a geometry which has been optimized

TABLE II. Numerical grid parameters for the calculated cases.

| Case | $L_x/\delta$ | $L_z/\delta$ | $L_x^+$ | $L_z^+$ | $N_x\times N_y\times N_z$ | $\Delta x^+\times\Delta y^+\times\Delta z^+$ |
|---|---|---|---|---|---|---|
| Straight T | 3.22 | 0.9312 | 580 | 168 | $16\times64\times128$ | $36\times(0.4-14)\times1.32$ |
| Short waves T | 3.22 | 0.9312 | 580 | 168 | $16\times64\times128$ | $36\times(0.4-14)\times1.32$ |
| Long waves T | 6 | 0.9312 | 1080 | 168 | $32\times64\times128$ | $33\times(0.4-14)\times1.32$ |
| Straight B | 3.22 | 0.7264 | 580 | 131 | $16\times64\times128$ | $36\times(0.4-14)\times1.03$ |
| Short waves B | 3.22 | 0.7264 | 580 | 131 | $16\times64\times128$ | $36\times(0.4-14)\times1.03$ |
| Long waves B | 6 | 0.7264 | 1080 | 131 | $32\times64\times128$ | $33\times(0.4-14)\times1.03$ |

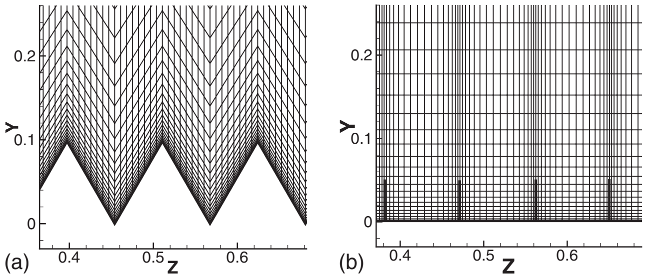

FIG. 8. Transverse view of the numerical grid. (a) Triangular riblets. (b) Knife-blade riblets.

for skin friction reduction with straight riblets.[7] The size of the computational domain was chosen based on the recommendations of Choi *et al.*[20] who performed direct numerical simulation (DNS) of straight triangular riblets with the similar Reynolds number Re=2800. The spanwise extent of the present computational domain is one-half times larger than a minimal flow unit of Jiménez and Moin[21] to allow for the possible increase in the streak spacings due to riblets. The spanwise extent of the domain allows for the simulation of eight riblets, and riblet-averaged results are presented. The resolution is equal to the DNS resolution of Ref. 20 in streamwise and spanwise directions, and it is only slightly lower in vertical direction, where Van Driest[22] wall functions are used. A transverse view of the numerical grid in the vicinity of the riblets is shown in Fig. 8 for both triangular and knife-blade riblet surfaces. We employ the incompressible formulation of the CODE_SATURNE (Ref. 23) to perform the simulations. CODE_SATURNE is an unstructured fully conservative finite-volume code of second order accuracy in time and space. The Smagorinsky[24] model is used as a subgrid-scale turbulence model. Further details of the simulations can be found in Peet *et al.*[25] The present simulations were validated for the case of a turbulent plane channel flow in Peet *et al.*[26] (versus DNS of Abe *et al.*[27]) and for the case of a turbulent channel flow whose bottom wall was covered with straight triangular riblets in Peet *et al.*[25] (versus DNS of Choi *et al.*[20]).

The theoretical value of the surface-averaged skin friction coefficient $\overline{\overline{C_f}}^{\text{th}}$ given by Eq. (60) was evaluated using statistical flow information taken from LES, while the normalization parameter $\mathcal{A}$ was calculated using Eq. (59). Simulations were not performed on curvilinear orthogonal grids, but on rectilinear grids shown in Fig. 8, and LES data were interpolated from the numerical grids of Fig. 8 to the curvilinear orthogonal grids of Fig. 5 in order to perform integrations in Eqs. (61) and (B4) for asymmetric and turbulent terms. We can also compute the skin friction coefficient directly as

$$\overline{\overline{C_f}}^{\text{comp}} = -\frac{2}{\mathrm{Re}U_r^2 s\lambda}\int_{A_w}\int \frac{\partial \bar{u}}{\partial n} dA_w, \qquad (64)$$

where $A_w$ is the wall surface. We use the bulk velocity $U_b$ as the reference velocity $U_r$ in Eqs. (60) and (64).

Both theoretical and computed values of skin friction coefficient as well as their relative difference $\epsilon=(\overline{\overline{C_f}}^{\text{comp}}-\overline{\overline{C_f}}^{\text{th}})/\overline{\overline{C_f}}^{\text{comp}}$ are listed in Table III. We also list an empirical value of the skin friction coefficient obtained from Dean's correlation for a turbulent flow over a flat plate for the same Reynolds number. The difference between the theoretical and computed values constitutes less than 4% for all the calculated cases. It can be noticed that the computed values of the skin friction coefficient are systematically larger than the theoretical values. The fact that the theoretical value for the skin friction coefficient on a flat plate is closer to the Dean's correlation than the computed value suggests that erroneous estimates come from Eq. (64) and not from the theoretical formula (60). In fact, estimating skin friction with Eq. (64) involves the knowledge of the exact slope of the velocity profile next to the wall, and it is well known that the near-wall quantities (and especially their gradients) are the most susceptible to approximation and modeling errors. It is believed that estimating skin friction by integrating Reynolds stresses via Eq. (60) (Reynolds stresses are fairly well predicted by LES, see comparison with DNS in Fig. 13 below and in Refs. 25 and 26) might be in general a more accurate way of extracting skin friction information from the simulations than direct computation via Eq. (64). Nonetheless, overestimation of skin friction values by Eq. (64) results in a systematic (and not irregular) error, and when the change in skin friction coefficient with the change in surface geometry is considered, the difference between the two estimation methods is very small (which is documented further in Table VI).

TABLE III. Comparison between theoretical and computed values of skin friction coefficient.

| Surface | Theoretical ($\overline{\overline{C_f}}^{\text{th}}$) | Computed ($\overline{\overline{C_f}}^{\text{comp}}$) | Difference ($\epsilon$) (%) | Dean's correlation |
|---|---|---|---|---|
| Flat | $8.59\times10^{-3}$ | $8.80\times10^{-3}$ | 2.4 | $8.49\times10^{-3}$ |
| Straight T | $8.08\times10^{-3}$ | $8.40\times10^{-3}$ | 3.8 | |
| Short waves T | $8.36\times10^{-3}$ | $8.54\times10^{-3}$ | 2.1 | |
| Long waves T | $8.02\times10^{-3}$ | $8.28\times10^{-3}$ | 3.1 | |
| Straight B | $7.63\times10^{-3}$ | $7.80\times10^{-3}$ | 2.2 | |
| Short waves B | $7.83\times10^{-3}$ | $8.05\times10^{-3}$ | 2.7 | |
| Long waves B | $7.46\times10^{-3}$ | $7.59\times10^{-3}$ | 1.7 | |

TABLE IV. Constituent contribution of different dynamical effects into skin friction, value of each term in Eq. (60).

| Surface | Bulk ($\overline{\overline{C}}_{fb}$) | Asymmetric ($\overline{\overline{C}}_{fa}$) | Turbulent ($\overline{\overline{C}}_{ft}$) | Total ($\overline{\overline{C}}_{f}$) |
|---|---|---|---|---|
| Flat | $2.20\times 10^{-3}$ | $0.008\times 10^{-3}$ | $6.39\times 10^{-3}$ | $8.59\times 10^{-3}$ |
| Straight T | $2.41\times 10^{-3}$ | $0.008\times 10^{-3}$ | $5.66\times 10^{-3}$ | $8.08\times 10^{-3}$ |
| Short waves T | $2.43\times 10^{-3}$ | $0.20\times 10^{-3}$ | $5.73\times 10^{-3}$ | $8.36\times 10^{-3}$ |
| Long waves T | $2.43\times 10^{-3}$ | $0.10\times 10^{-3}$ | $5.49\times 10^{-3}$ | $8.02\times 10^{-3}$ |
| Straight B | $2.36\times 10^{-3}$ | $0.03\times 10^{-3}$ | $5.24\times 10^{-3}$ | $7.63\times 10^{-3}$ |
| Short waves B | $2.38\times 10^{-3}$ | $0.11\times 10^{-3}$ | $5.34\times 10^{-3}$ | $7.83\times 10^{-3}$ |
| Long waves B | $2.38\times 10^{-3}$ | $0.006\times 10^{-3}$ | $5.07\times 10^{-3}$ | $7.46\times 10^{-3}$ |

### *4. Constituent contributions*

It is seen from Table III that skin friction for riblet surfaces is smaller than skin friction for a flat surface for all the calculated cases, proving that riblets are an effective method of skin friction reduction provided that riblet geometry parameters are chosen correctly. Wavy riblets were introduced in an attempt to achieve additional skin friction reduction benefits over straight riblets.[17,25] Table III shows that these additional benefits are achieved for wavy riblets with longer wavelengths but are not achieved for short wavy riblets. The current theoretical approach allows us to give more insight into the skin friction reduction mechanism for riblet-covered surfaces and explain the difference in skin friction reduction properties of short and long wavy riblets by looking at the quantitative contribution of different dynamical effects to the total skin friction coefficient.

The constituent contribution of different dynamical effects to the skin friction is shown in Table IV and represents the value of each individual term in Eq. (60) (bulk $\overline{\overline{C}}_{fb}$, asymmetric $\overline{\overline{C}}_{fa}$, turbulent $\overline{\overline{C}}_{ft}$, and total $\overline{\overline{C}}_{f}$—their sum). In order to better understand the relative effect of each term, we also look at the ratio of each component (and their sum) to the total skin friction coefficient of a flat surface $\overline{\overline{C}}_{f}^{f}$ in Table V. In the remainder of this section, we analyze each term contributing to the skin friction coefficient in more detail in order to understand the differences in the skin friction reduction properties between the different riblet surfaces.

### *5. Bulk contribution*

The first term in Eq. (60), bulk contribution, is calculated as

$$\overline{\overline{C}}_{fb} = \frac{2U_b A_\Sigma \mathcal{I}}{\mathrm{Re}\, U_r^2 \mathcal{A}s}, \qquad (65)$$

where

$$\mathcal{I} = \int_0^\lambda \frac{1}{\lambda \cos \beta} dx$$

[cf. Eqs. (60) and (B2)]. Since for both straight and wavy riblets the $y$-$z$ cross-sectional area $A_\Sigma$ is the same at every streamwise location, it was taken out of the integral in $x$.

*a. Straight riblets.* For straight riblets, the integral $\mathcal{I}=\int_0^\lambda 1/(\lambda \cos \beta)dx=1$ and, therefore, Eq. (65) becomes

$$\overline{\overline{C}}_{fb} = \frac{2U_b A_\Sigma}{\mathrm{Re}\, U_r^2 \mathcal{A}s}. \qquad (66)$$

Laminar flow over straight riblets (which are streamwise-homogeneous surfaces with symmetric cross-section) is symmetric with respect to the $x$-$y$ center plane. Therefore, the asymmetric term for a laminar flow over straight riblets is identically zero, since symmetric positive and negative contributions cancel each other during cross-sectional averaging. Furthermore, turbulent contribution in a laminar flow is identically zero, and bulk term defined by Eq. (66) is the only contribution to the laminar skin friction coefficient. There-

TABLE V. Ratio of each term in Eq. (60) to the total flat plate skin friction coefficient.

| Surface | Bulk ($\overline{\overline{C}}_{fb}/\overline{\overline{C}}_{f}^{f}$) | Asymmetric ($\overline{\overline{C}}_{fa}/\overline{\overline{C}}_{f}^{f}$) | Turbulent ($\overline{\overline{C}}_{ft}/\overline{\overline{C}}_{f}^{f}$) | Total ($\overline{\overline{C}}_{f}/\overline{\overline{C}}_{f}^{f}$) |
|---|---|---|---|---|
| Flat | 0.26 | 0 | 0.74 | 1 |
| Straight T | 0.28 | 0 | 0.66 | 0.94 |
| Short waves T | 0.28 | 0.02 | 0.67 | 0.97 |
| Long waves T | 0.28 | 0.01 | 0.64 | 0.93 |
| Straight B | 0.28 | 0 | 0.61 | 0.89 |
| Short waves B | 0.28 | 0.01 | 0.62 | 0.91 |
| Long waves B | 0.28 | 0 | 0.59 | 0.87 |

TABLE VI. Skin friction reduction value $R_f$.

| Surface | Theoretical (%) | Computed (%) |
|---|---|---|
| Straight T | 6 | 5 |
| Short waves T | 3 | 3 |
| Long waves T | 7 | 6 |
| Straight B | 11 | 11 |
| Short waves B | 9 | 9 |
| Long waves B | 13 | 14 |

fore, for symmetric surfaces, the bulk contribution represents a skin friction coefficient which would develop in a laminar flow over the same surface, $\overline{\overline{C}}_{fb}=\overline{\overline{C}}_{f\mathrm{lam}}$.

Equations (59) and (66) provide a way of exact computation of the skin friction coefficient in a laminar flow for symmetric streamwise-homogeneous surfaces based on purely geometrical considerations without performing the flow calculations. [Remember that Eq. (59) is exact for laminar streamwise-homogeneous flows.] Thus, according to Eq. (66), the ratio of the laminar skin friction coefficient on a surface with straight riblets $\overline{\overline{C}}^r_{f\mathrm{lam}}$ to a laminar skin friction coefficient on a flat surface $\overline{\overline{C}}^f_{f\mathrm{lam}}$ can be estimated as

$$\overline{\overline{C}}^r_{f\mathrm{lam}}/\overline{\overline{C}}^f_{f\mathrm{lam}}=\mathcal{A}^f/\mathcal{A}^r \tag{67}$$

if $(U_bA_\Sigma)/(\mathrm{Re}U_r^2s)$ is the same for both surfaces. According to Eq. (53), $\mathcal{A}^f=\delta^2/3$ for a flat surface. Calculating $\mathcal{A}^r$ with Eq. (59) allows us to compute the ratio $\overline{\overline{C}}^r_{f\mathrm{lam}}/\overline{\overline{C}}^f_{f\mathrm{lam}}$. Variation in $\overline{\overline{C}}^r_{f\mathrm{lam}}/\overline{\overline{C}}^f_{f\mathrm{lam}}$ with riblet spacing $s/\delta$ calculated with Eq. (67) is shown in Fig. 9 for two triangular riblet surfaces with different ridge angles $\alpha$ and for two knife-blade riblet surfaces with different height-to-spacing ratios $h/s$. We chose height-to-spacing ratios $h/s$ for knife-blade riblets to be equal to the $h/s$ ratios of the triangular riblets. Note that although we vary $s/\delta$, the ratio $A_\Sigma/s$, and so $(U_bA_\Sigma)/(\mathrm{Re}U_r^2s)$, stay the same, since $A_\Sigma=\delta s$ and $\delta$ is not varied. Values of $\overline{\overline{C}}^r_{f\mathrm{lam}}/\overline{\overline{C}}^f_{f\mathrm{lam}}$ obtained by Choi *et al.*[28] for straight triangular riblets from numerical solution of governing flow equations are also shown for comparison. They agree well with the values found with the proposed geometrical method. It is seen that in a laminar flow skin friction on a riblet surface is larger than that on a flat surface. The reason for that is the larger wetted surface area of a riblet surface compared to a flat surface, which can be characterized by a parameter $L_w/s$ ($L_w$ is the length of the wall segment $\partial\Sigma_w$). Values of $L_w/s$ are listed in a caption to Fig. 9 for each riblet case, $L_w/s=1$ for a flat surface. It is seen that skin friction is indeed increased with the increase in $L_w/s$. It is interesting to note that triangular riblets with $\alpha=60°$ and knife-blade riblets with $h/s=0.5$, both having the same value of $L_w/s=2$, show almost identical skin friction, suggesting that skin friction drag in a laminar flow over straight riblets indeed scales with $L_w/s$.

Since $\overline{\overline{C}}_{fb}=\overline{\overline{C}}_{f\mathrm{lam}}$ for symmetric surfaces, the ratio of bulk terms $\overline{\overline{C}}^r_{fb}/\overline{\overline{C}}^f_{fb}$ from turbulent flow simulations should equal to $\overline{\overline{C}}^r_{f\mathrm{lam}}/\overline{\overline{C}}^f_{f\mathrm{lam}}$ for straight riblets. Indeed we get the ratio of $\overline{\overline{C}}^r_{fb}/\overline{\overline{C}}^f_{fb}=1.1$ for straight triangular riblets ($\alpha=60°$, $s/\delta=0.1164$) and $\overline{\overline{C}}^r_{fb}/\overline{\overline{C}}^f_{fb}=1.07$ for straight knife-blade riblets ($h/s=0.5$, $s/\delta=0.0908$), which, as can be seen from Fig. 9, does conform to the corresponding ratio of the laminar coefficients.

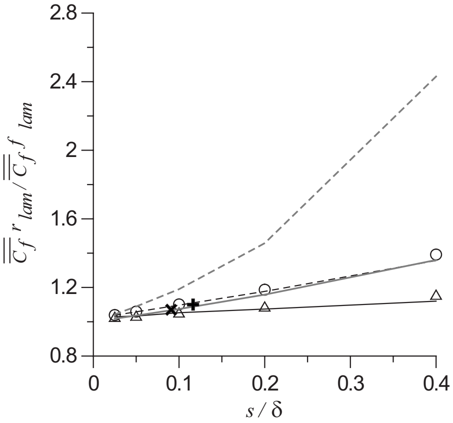

FIG. 9. Variation in skin friction ratio $\overline{\overline{C}}^r_{f\mathrm{lam}}/\overline{\overline{C}}^f_{f\mathrm{lam}}$ for straight riblets with respect to a riblet spacing. Black lines, triangular riblets, Eq. (67): solid line, $\alpha=45°$, $h/s=0.5$, $L_w/s=1.4$; dashed line, $\alpha=60°$, $h/s=0.866$, $L_w/s=2$. Grey lines, knife-blade riblets, Eq. (67): solid line, $h/s=0.5$, $L_w/s=2$; dashed line, $h/s=0.866$, $L_w/s=2.732$. Symbols: △, triangular riblets with $\alpha=45°$, Choi *et al.* (Ref. 28); ○, triangular riblets with $\alpha=60°$, Choi *et al.* (Ref. 28); +, $\overline{\overline{C}}^r_{fb}/\overline{\overline{C}}^f_{fb}$, triangular riblets with $\alpha=60°$, current LES; ×, $\overline{\overline{C}}^r_{fb}/\overline{\overline{C}}^f_{fb}$, knife-blade riblets with $h/s=0.5$, current LES.

*b. Wavy riblets.* For wavy riblets, the integral $\mathcal{I}=\int_0^\lambda 1/(\lambda\cos\beta)dx$ is no longer unity. But for the case of periodic sinusoidal waves defined by Eq. (54) the integral $\mathcal{I}$ can be taken analytically. Indeed, from Eqs. (54) and (55) it follows that

$$\frac{1}{\cos\beta(x)}=\sqrt{\left(\frac{2\pi a}{\lambda}\right)^2\cos^2\left(\frac{2\pi}{\lambda}x\right)+1} \tag{68}$$

and

$$\begin{aligned}\mathcal{I}&=\int_0^\lambda\frac{1}{\lambda\cos\beta}dx\\&=\frac{2}{\pi}\sqrt{\left(\frac{2\pi a}{\lambda}\right)^2+1}\int_0^{\pi/2}\sqrt{1-k^2\sin^2\Phi}\,d\Phi\\&=\frac{2}{\pi}\frac{1}{\cos\beta_{\max}}E\left(k,\frac{\pi}{2}\right),\end{aligned} \tag{69}$$

where $\beta_{\max}=\arctan(2\pi a)/\lambda$, $k=\sin\beta_{\max}$, $E(k,\pi/2)$ is a complete elliptic integral of the second kind, and a substitution $\Phi=(2\pi x)/\lambda$ was made to evaluate the integral in Eq. (69).

Since $\mathcal{I}^{\mathrm{wavy}}>1$ and $\mathcal{I}^{\mathrm{straight}}=1$, the bulk term defined by Eq. (65) is always greater for the wavy riblets than for the straight riblets of the same geometry, and their ratio obeys

$$\overline{\overline{C}}^{\mathrm{wavy}}_{fb}/\overline{\overline{C}}^{\mathrm{straight}}_{fb}=\mathcal{I}^{\mathrm{wavy}}, \tag{70}$$

which is confirmed by Table IV. Note that the asymmetric term is not necessarily zero for a laminar flow over wavy riblets, since the flow is no longer symmetric. Therefore, the

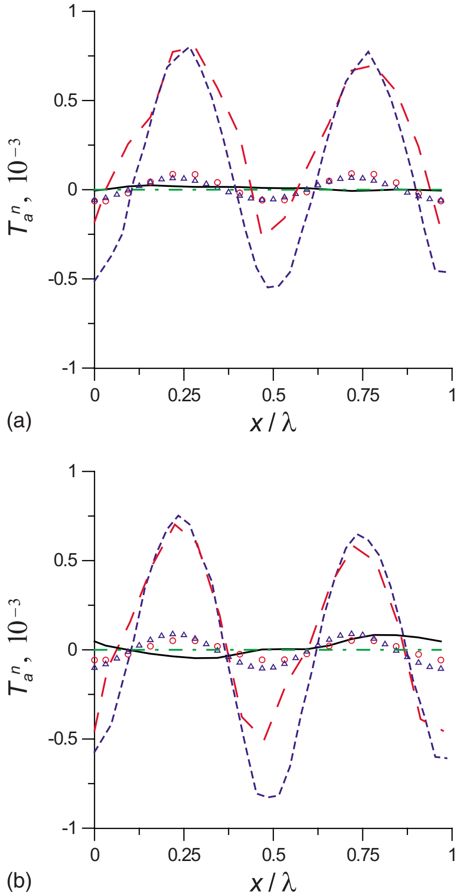

FIG. 10. (Color online) Streamwise dependence of asymmetric contribution $\mathcal{T}_a^n(x)$ for straight and wavy riblets. Laminar case: –·–, straight; △, short waves; ○, long waves. Turbulent case: ———, straight; — — —, short waves; – – –, long waves. (a) Triangular riblets. (b) Knife-blade riblets.

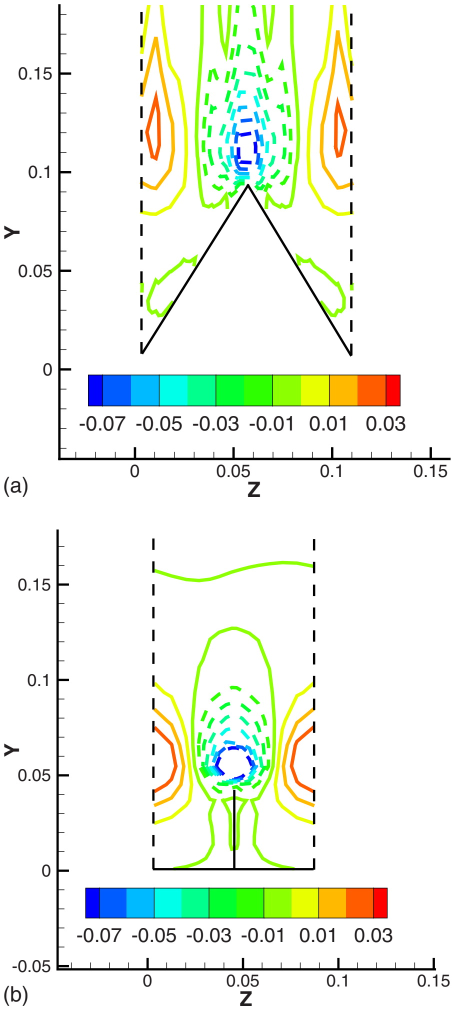

FIG. 11. (Color online) Cross-sectional view of the local asymmetric term $\mathcal{I}^n_{xr}(x,y,z)$ for straight riblets in a turbulent case. Solid lines, positive values; dashed lines, negative values. Contour increment: 0.01. (a) Triangular riblets. (b) Knife-blade riblets.

bulk term does not correspond exactly to the laminar skin friction coefficient for surfaces invoking asymmetric flow. However, since the asymmetric term is usually small in a laminar flow, the bulk term will be close to $\overline{\overline{C}}_{f\mathrm{lam}}$ even for asymmetric cases. In a turbulent flow, on the other hand, the bulk term constitutes only about a quarter of the total skin friction coefficient $\overline{\overline{C}}_f$ for both straight and wavy triangular and knife-blade riblets, as can be seen from Table V.

### *6. Asymmetric contribution*

The asymmetric contribution

$$\overline{\overline{C}}_{fa} = \frac{1}{U_r^2 \mathcal{A} s \lambda} \int_0^\lambda \frac{\mathcal{T}_a}{\cos \beta} dx \qquad (71)$$

is due to the flow asymmetry and can be present in both laminar and turbulent cases if the flow is asymmetric. For periodic riblets, where the asymmetric term $\mathcal{T}_a$ is defined by Eq. (62), it represents the effect of a mean crossflow asymmetry on skin friction. Streamwise variation in the local normalized asymmetric term $\mathcal{T}_a^n(x) = \mathcal{T}_a(x)/[U_r^2 \mathcal{A} s \cos \beta(x)]$ is plotted in Fig. 10. The laminar case is also plotted for reference.

*a. Straight riblets.* For the straight riblets, the asymmetric term $\mathcal{T}_a^n(x)$ is zero at each streamwise location both for the laminar and turbulent cases (the slight deviation from zero in the case of turbulent straight knife-blade riblets most likely comes from numerical errors) since, as discussed earlier, symmetric positive and negative crossflow contributions cancel each other during cross-sectional averaging. Cross-sectional symmetry of the asymmetric term for straight riblets in a turbulent case can be viewed in Fig. 11, where the integrand of Eq. (61) normalized by $U_r^2 \mathcal{A} s \cos \beta / A_\Sigma$,

$$\mathcal{I}^n_{xr}(x,y,z) = \frac{A_\Sigma}{U_r^2 \mathcal{A} s \cos \beta(x)} (\gamma(\eta^{\mathrm{top}}) - \gamma(\eta))^2 (-I''_{xr}(x,y,z)), \qquad (72)$$

is plotted.

*b. Wavy riblets.* For the wavy riblets, the asymmetric term $\mathcal{T}_a^n(x)$ is no longer zero at each streamwise location due to the mean crossflow asymmetry and a lack of cancellation. Streamwise dependence of the asymmetric term resembles periodic oscillations with about twice the frequency of riblet shape oscillations and the peak values of $1 \times 10^{-3}$ in the turbulent case and $0.1 \times 10^{-3}$ in the laminar case. Note that as mentioned earlier, the local asymmetric term is not identi-

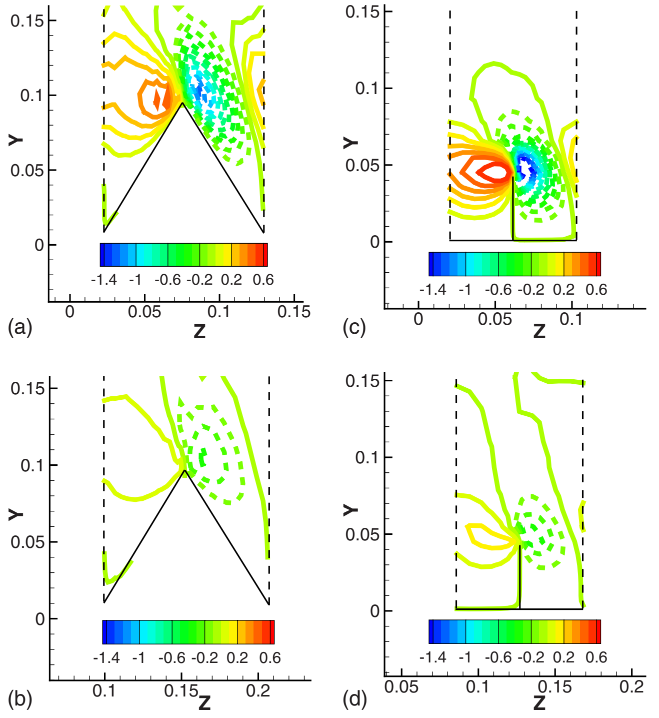

FIG. 12. (Color online) Cross-sectional view of the local asymmetric term $\mathcal{I}_{xr}^{n}(x,y,z)$ for short wavy riblets in a turbulent case. Solid lines, positive values; dashed lines, negative values. Contour increment: 0.1. (a) Triangular riblets, $x/\lambda \sim 0$. (b) Triangular riblets, $x/\lambda \sim 1/4$. (c) Knife-blade riblets, $x/\lambda \sim 0$. (d) Knife-blade riblets, $x/\lambda \sim 1/4$.

cally zero in the laminar case for wavy riblets, although it is significantly smaller than its turbulent counterpart. As seen from Fig. 10, the asymmetric term oscillations resemble perfect sinusoidal waves for the laminar wavy cases resulting in a zero streamwise average. However, for turbulent cases, the curves are shifted upward resulting in a slightly positive streamwise-averaged value of the asymmetric term. The upward shift is more pronounced for short oscillation wavelengths and it is smaller for longer oscillation wavelengths. Also, the upward shift seems to be larger for triangular riblets resulting in 2% and 1% of the asymmetric contribution for short and long wavelengths, respectively, while it is only 1% and 0% for knife-blade riblets. This might be connected to the fact that the oscillation slope $\beta_{\max}=9.6°$ is smaller for the knife-blade riblets than $\beta_{\max}=11.3°$ for the triangular riblets. It is hypothesized that the larger value of the asymmetric term for smaller wavelengths is associated with the higher excitation of a riblet boundary layer when the oscillation period is too short. A cross-sectional view of the local asymmetric term $\mathcal{I}_{xr}^{n}(x,y,z)$ defined by Eq. (72) is plotted in Fig. 12 for triangular and knife-blade short wavy riblets in the turbulent case at two streamwise locations: $x/\lambda=0$ corresponding to the minimum $\mathcal{T}_a^n$ value and $x/\lambda=1/4$ corresponding to the maximum value. When $x/\lambda=0$, the mean spanwise velocity in the riblet boundary layer is maximum, and local values of the asymmetric term $\mathcal{I}_{xr}^{n}$ are also the largest. When $x/\lambda=1/4$, the mean spanwise velocity is zero since the mean flow in a riblet boundary layer is parallel to the incoming stream, and local values of the asymmetric term are the smallest. Note that $\mathcal{T}_a^n$ is actually maximum when the local values of $\mathcal{I}_{xr}^{n}$ are the smallest (at $x/\lambda=1/4,3/4,\ldots$), and vice versa, showing that it is the cross-sectional average and not the local values that determine the contribution of asymmetric effects to the spanwise-averaged skin friction drag. A cross-sectional view of $\mathcal{I}_{xr}^{n}$ for long wavelengths is similar and is not plotted here.

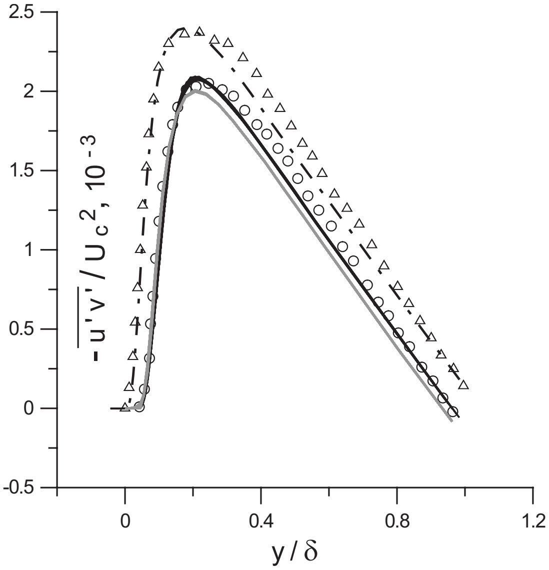

FIG. 13. Distribution of turbulent shear stress $-\overline{u'v'}/U_c^2$ across the channel. Black solid lines, triangular riblets; grey solid lines, knife-blade riblets; black dashed-dotted line, above a flat surface. Symbols, DNS of Choi *et al.* (Ref. 20): ○, triangular riblets, above a riblet tip; △, above a flat plate.

### *7. Turbulent contribution*

Turbulent component

$$\overline{\overline{C}}_{ft}=\frac{1}{U_r^2\mathcal{A}s\lambda}\int_0^{\lambda}\frac{\mathcal{T}_t}{\cos\beta}dx \tag{73}$$

is definitely the major contribution to the skin friction coefficient in a turbulent flow and is responsible for almost three quarters of its total value (see Table V).

*a. Straight riblets.* The turbulent contribution is significantly lower for a flow over straight riblets than for a flow over a flat plate. Knife-blade riblets show larger reduction in turbulent contribution with respect to a flat plate (13%) than triangular riblets (8%), as seen from Tables IV and V. Distribution of the streamwise-averaged turbulent shear stress $-\overline{u'v'}/U_c^2$ over the vertical lines across the channel cross-section is shown in Fig. 13 for straight triangular and knife-blade riblets in comparison with the shear stress above a flat surface. Data from DNS of Choi *et al.*[20] for straight triangular riblets of a similar configuration with Re=2800 are also plotted for reference. We plot the turbulent stress values normalized by the centerline velocity $U_c$, and not by the reference velocity $U_r=U_b$, to conform to the data of Choi *et al.*[20] It is clearly seen that turbulent shear stress is suppressed over the entire range of $y/\delta$ for riblet surfaces with respect to a flat surface and that the knife-blade riblet surface exhibits further reduction in $-\overline{u'v'}$ over the triangular riblet surface.

Turbulence reduction by straight riblets of favorable geometry was previously documented in the literature.[6,7]

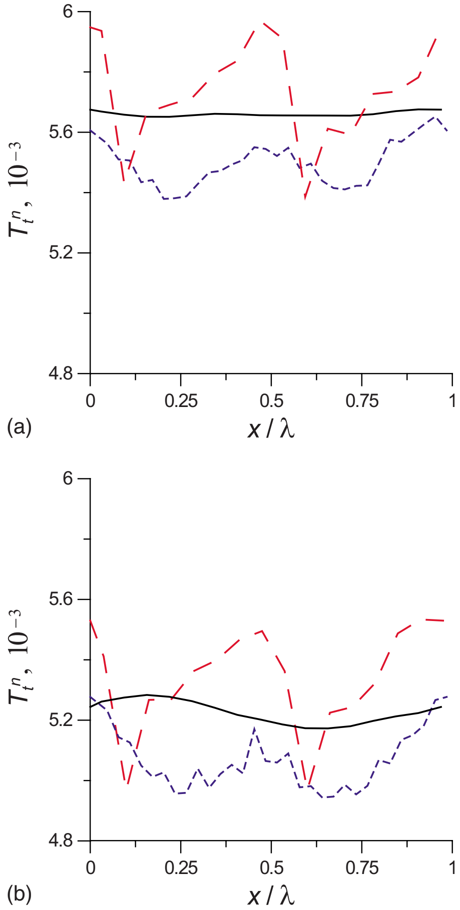

FIG. 14. (Color online) Streamwise dependence of turbulent contribution $\mathcal{T}_t^n(x)$ for straight and wavy riblets. ———, Straight riblets; — — —, short wavy riblets; – – –, long wavy riblets. (a) Triangular riblets. (b) Knife-blade riblets.

Namely, it was shown that riblets are able to displace coherent streamwise vortices, which naturally form in the turbulent boundary layer, away from the wall, thus leading to a decrease in turbulent momentum transfer and turbulent shear stress near the wall.[3,20,29] It is also a known fact that knife-blade riblets represent the most efficient geometry among all other riblet surfaces for displacing coherent vortices away from the wall[7] and thus exhibit the largest values of turbulence reduction.

*b. Wavy riblets.* For wavy riblets with long wavelengths, both for triangular and knife-blade cases, further turbulent reduction with respect to the corresponding straight riblet surface is observed resulting in 2% decrease in turbulent contribution to skin friction (see Tables IV and V). However, for the short wavelengths, a slight increase in turbulent contribution (by 1%) is documented both in triangular and knife-blade cases. Streamwise variation in the local turbulent term $\mathcal{T}_t^n(x)=\mathcal{T}_t(x)/[U_r^2\mathcal{A}s\cos\beta(x)]$ for straight and wavy riblets is plotted in Fig. 14. As expected, streamwise variation for the straight riblets is practically absent (slight variation for straight knife-blade riblets is likely due to numerical uncertainties). The situation is quite different for wavy riblets. For the short riblets, both triangular and knife-blade, the same well-defined pattern is observed, where the turbulent term gradually rises to its maximum value reached at every half-period, and then drops abruptly to its minimum value. As compared to the straight riblets, the overall levels of the turbulent component $\mathcal{T}_t^n(x)$ are reduced for the long wavy riblets, whereas maximum values of $\mathcal{T}_t^n(x)$ are larger and minimum values are smaller for the short wavy riblets than the corresponding straight riblet values. It is possible that for wavy riblets with sufficiently large wavelength, by analogy with a spanwise-oscillating wall, spanwise motion in a wavy-riblet boundary layer leads to a spanwise displacement of coherent vortices with respect to the low-speed streaks in addition to their vertical displacement, which violates their spatial coherence, weakens the near-wall burst activity, and reduces turbulent shear stress levels even further with respect to nonoscillating riblets. It is most likely that for short wavelengths the oscillations are too rapid and there is not enough time for the turbulence to reach a local equilibrium state, so that the turbulence fluctuations show large streamwise intermittency and the streamwise-averaged contribution $\overline{\overline{C}}_{ft}$ is increased compared to the straight riblets. In fact, the optimum oscillation frequency for skin friction reduction with spanwise wall oscillation is reported to be about $T^+\simeq 100$.[10,30,31] If, for a riblet boundary layer, we estimate convection velocity to be $c^+\simeq 10$ at $y^+\simeq 10$ (Ref. 32) (where the spanwise motion due to the protrusion of riblets is maximum), the oscillation period for the long wavy riblets with $\lambda^+\simeq 1000$ is $T^+=\lambda^+/c^+\simeq 100$, close to the reported wall-oscillation optimum, so that the favorable effects of spanwise motion on skin friction reduction are the largest. For the short wavy riblets with $\lambda^+\simeq 600$ the frequency is larger, corresponding to a smaller period of $T^+\simeq 60$, for which skin friction reduction with spanwise wall motion is much smaller,[30] which might be explained by similar nonequilibrium effects in a spanwise-oscillating wall layer as those observed in the current study for short wavy riblets.

### *8. Skin friction drag reduction*

The skin friction drag reduction value defined as $R_f=(\overline{\overline{C}}_f^f-\overline{\overline{C}}_f^r)/\overline{\overline{C}}_f^f$, predicted by the theoretical formula [Eq. (60)] and by direct computation [Eq. (64)], is cited in Table VI for the six calculated cases. Here $\overline{\overline{C}}_f^f$ is the skin friction coefficient of a flat surface and $\overline{\overline{C}}_f^r$ is the skin friction coefficient of a riblet surface. As discussed above, although the values of $\overline{\overline{C}}_f^{\text{comp}}$ obtained from Eq. (64) are larger by 2%–4% than the corresponding values $\overline{\overline{C}}_f^{\text{th}}$ predicted by the theoretical formula (cf. Table III), this seems to be a systematic error, and the values of change in skin friction with the change in surface geometry (skin friction drag reduction) differ much less (see Table VI). Decomposition of the skin friction coefficient into constituent contributions discussed above allows us to explain the skin friction reduction mechanism of straight and wavy riblets and clarify why short and long wavy riblets have such different skin friction reduction properties.

*a. Straight riblets.* For the straight riblets (cf. Table V), two terms come into play: the bulk term and the turbulent term. Although the bulk term is increased slightly from 26% to 28% for straight riblets as compared to a flat surface, significant reduction in the turbulent term (from 74% to 66% for triangular riblets and to 61% for knife-blade riblets) overcomes the 2% increase in the bulk term resulting in 6% skin friction reduction for triangular riblets and 11% skin friction reduction for knife-blade riblets. Those values are in good agreement with the skin friction reduction values published in the open literature for those configurations. Furthermore, the accepted hypothesis that skin friction on a straight riblet surface is reduced due to a favorable interaction of riblets with the near-wall turbulence is confirmed, as well as the fact that knife-blade riblets possess smaller skin friction than riblets with triangular cross-section because they are more effective in reducing the near-wall turbulence.

*b. Wavy riblets.* For the wavy riblets, the situation is slightly more complicated, since a delicate balance between small changes in all the three terms determines a positive or negative increment of skin friction with respect to straight riblets. Indeed, the bulk contribution is very slightly increased for wavy riblets due to the bulk flow oscillations and nonunity of $\cos \beta$; the asymmetric contribution is also slightly increased (especially for the short wavelengths); but the turbulent contribution is slightly decreased for the long wavelengths and slightly increased for the short wavelengths. As a result, long wavy riblets exhibit smaller $C_f$ values than their straight riblet counterparts, while short wavy riblets exhibit larger $C_f$ values. For long wavy riblets, a skin friction increase due to the asymmetric term is very small (1% for triangular, ~0% for knife-blade), whereas the decrease in turbulence intensity by spanwise oscillations is 2% with respect to straight riblets, resulting in a positive net effect of riblet oscillations on skin friction reduction. However, if the wavelength of the oscillations is too small (or frequency is too high), smooth transition of the flow between the different phases of oscillation no longer occurs, and the local turbulence does not have enough time to adjust to a change in the spanwise flow direction and is constantly in an excited and locally nonequilibrium state. This leads to asymmetries in the streamwise distribution of the asymmetric term and large streamwise fluctuations of the turbulent term seen in Figs. 10 and 14. Thus, increase in both the asymmetric contribution (by 1%–2%) and the turbulent contribution (by 1%) occurs in short wavy riblets, resulting in a higher skin friction coefficient than that over straight riblets. To summarize, introducing spanwise oscillations to the conventional (straight) riblet shape does produce additional skin friction reduction benefits, provided the wavelength of oscillations is not too small.

Promising results on skin friction reduction by long wavy riblets suggest that it might be beneficial to use wavy riblet surfaces for drag reduction in practical applications. One has to be careful, however, since pressure drag becomes nonzero for wavy surfaces, since the local surface normal is no longer always perpendicular to the free-stream flow direction. It was estimated by Peet *et al.*[18] that the pressure drag for the wavy riblet configurations considered in this paper is about 2% (it was shown to be proportional to the square of the oscillation slope $\tan^2 \beta_{\max}$ and not depending on the cross-sectional shape). Parametric study of drag reduction with wavy riblets versus oscillation parameters revealed that total drag reduction benefits (accounting for both skin friction and pressure drag) of at least 3% compared to straight riblets are still possible for optimum configurations.[18] Wavy riblets can therefore be a promising method of achieving high values of drag reduction by simple and inexpensive geometrical surface modifications. Benefits might be even larger for higher Reynolds numbers relevant to practical applications.

## IV. CONCLUSIONS

An analytical formula is derived for the turbulent skin friction coefficient on geometrically complex surfaces, whose shape satisfies certain conditions. Analytical expression for the skin friction coefficient is thus given for streamwise and spanwise homogeneous surfaces of any shape, as well as some more complex configurations including wavy patterns. The derivation consists of integrating the governing equations of motion and leads to a closed-form expression between the skin friction coefficient and statistical information in the flow above the surface. The expression shows that contribution to skin friction can be decomposed into several terms: bulk, asymmetric, pressure, transient, and turbulent. The derived expression can be particularly useful for analyzing the skin friction drag reduction properties of various surfaces. The analytical formula is validated for a flat plate and for a surface covered with straight and wavy riblets of triangular and knife-blade cross-sections by comparing skin friction computed directly as an integral of the wall velocity gradient with the prediction of the formula. A difference of no more than 4% is reported for all the simulated cases, which comes from a systematic error in LES estimation of the local wall velocity gradients. Analysis of different dynamical effects contributing to the total skin friction value for riblet-covered surfaces shows the following:

(1) The bulk contribution is slightly larger for straight riblet surfaces than for a flat surface, and even larger for wavy riblet surfaces.

(2) The asymmetric contribution is zero for a flat plate and for straight riblets, but not zero for wavy riblets in both laminar and turbulent cases. The asymmetric contribution is generally larger for short riblets versus long riblets and for triangular riblets versus knife-blade riblets. In the turbulent case, the maximum value is 2% for short triangular riblets, and the minimum value is ~0% for long knife-blade riblets. The percentage signifies the fraction of each particular term with respect to the total skin friction of a flat surface, $\overline{\overline{C_f}}^f$.

(3) The turbulent contribution is reduced by 8% for straight triangular riblets as compared to a flat surface, with even further reduction of up to 13% for straight knife-blade riblets. Further reduction by 2% is documented for long wavy riblets as compared to the straight riblets with the same cross-section, but an increase of 1% is observed for short wavy riblets. The turbulent term exhibits large

fluctuations with respect to a streamwise coordinate for short wavy riblets, and those fluctuations are much reduced for long wavy riblets.

Skin friction reduction values of 6% and 11% for straight triangular and knife-blade riblets, respectively, are documented and are in agreement with the published literature.[7,20] It is found that further skin friction reduction is achieved for wavy riblets with large oscillation wavelength due to additional turbulence suppression by spanwise motion. The mechanism for the additional turbulence suppression most likely consists of tilting streamwise vortices and violating their spatial coherence with respect to the low-speed streaks, similar to the effects found in a spanwise-oscillating wall.[10] If the oscillation wavelength is too small, however, skin friction is increased with respect to the straight riblets due to nonequilibrium effects leading to large streamwise fluctuations of the turbulent term and increase in both the turbulent and asymmetric terms. Knife-blade riblets are confirmed to be more efficient in skin friction reduction than triangular riblets for a straight riblet configuration. Knife-blade riblets are also more efficient in bringing out the benefits from a spanwise shape oscillation: knife-blade wavy riblets show larger values of skin friction reduction with respect to straight riblets compared to triangular wavy riblets.

Wavy riblets represent a promising way of reducing skin friction drag on the surfaces in contact with a turbulent flow at practically no cost and they are more efficient than straight riblets. Wavy riblets might work even better for higher Reynolds numbers. Even when pressure drag is taken into account, the total drag reduction benefits of several percent in comparison with straight riblets can be achieved for optimum configurations.[18] The wavelength of the oscillations should be carefully chosen, however, and should not be made too small.

## ACKNOWLEDGMENTS

This work was supported by the Agence Nationale pour la Recherche (ANR) of France under the project PAN-H/READY. The authors also wish to thank Dr. Yves Charron for his valuable input.

## APPENDIX A: LOCAL SKIN FRICTION DRAG

In this appendix, we show that the local skin friction drag defined by Eq. (3) can be expressed by Eq. (4). To do that, we extend $(\nabla\otimes\vec{v}+(\nabla\otimes\vec{v})^T)\vec{n}\cdot\vec{i}$ as

$$
\begin{aligned}
[\nabla\otimes\vec{v}+(\nabla\otimes\vec{v}]^T)\vec{n}\cdot\vec{i} &= \left(\begin{bmatrix} 2\dfrac{\partial u}{\partial x} & \dfrac{\partial v}{\partial x}+\dfrac{\partial u}{\partial y} & \dfrac{\partial w}{\partial x}+\dfrac{\partial u}{\partial z} \\ \dfrac{\partial u}{\partial y}+\dfrac{\partial v}{\partial x} & 2\dfrac{\partial v}{\partial y} & \dfrac{\partial w}{\partial y}+\dfrac{\partial v}{\partial z} \\ \dfrac{\partial u}{\partial z}+\dfrac{\partial w}{\partial x} & \dfrac{\partial v}{\partial z}+\dfrac{\partial w}{\partial y} & 2\dfrac{\partial w}{\partial z} \end{bmatrix} \begin{bmatrix} n_x \\ n_y \\ n_z \end{bmatrix}\right)^T \cdot \begin{bmatrix} 1 \\ 0 \\ 0 \end{bmatrix} \\
&= \left(\frac{\partial u}{\partial x}n_x+\frac{\partial u}{\partial y}n_y+\frac{\partial u}{\partial z}n_z\right)+\left(\frac{\partial u}{\partial x}n_x+\frac{\partial v}{\partial x}n_y+\frac{\partial w}{\partial x}n_z\right) \\
&= \frac{\partial u}{\partial n}+\frac{\partial(\vec{v}\cdot\vec{n})}{\partial x}=\frac{\partial u}{\partial n}+\frac{\partial v_n}{\partial x},
\end{aligned}
\tag{A1}
$$

which, if substituted to Eq. (3), leads to Eq. (4).

## APPENDIX B: TRANSFORMATION OF TERMS

In this appendix, we spell out the formulas obtained for the four terms of Eq. (50) after the double integration $\int_0^{\eta^{\mathrm{top}}} d\gamma \int_0^{\eta} d\gamma$ and summation over $d\zeta\to 0$ is applied to this equation. As before, $\gamma$ denotes the local variable along the integration contour, and $d\gamma$ its differential. We will also be using the notations $\gamma(\eta)$ and $\gamma(\zeta)$ to distinguish the integration along $\eta$ or $\zeta$ lines, and $d\gamma(\eta)$, $d\gamma(\zeta)$ referring to their differentials. The transformation of the four terms can be written as follows:

$$
\begin{aligned}
&\lim_{d\zeta\to 0}\sum_{d\zeta}\int_0^{\eta^{\mathrm{top}}} d\gamma(\eta)\int_0^{\eta} d\gamma(\eta) \\
&\quad\times\int_{\partial\sigma_w}\left\{w[\gamma(\zeta)]\frac{d\gamma(\zeta)}{s}-\frac{dA_\sigma(\eta,\zeta)}{A_\Sigma}\right\} \\
&\quad=\int_{\zeta_1}^{\zeta_2}\int_0^{\eta^{\mathrm{top}}}[\gamma(\eta^{\mathrm{top}})-\gamma(\eta)] \\
&\quad\quad\times\left\{w[\gamma(\zeta_w)]\frac{d\gamma(\zeta_w)}{s}-\frac{dA_\sigma(\eta,\zeta)}{A_\Sigma}\right\}d\gamma(\eta)=\mathcal{A},
\end{aligned}
\tag{B1}
$$

$$
\begin{aligned}
&\lim_{d\zeta\to 0}\sum_{d\zeta}\frac{2}{\mathrm{Re}}\int_0^{\eta^{\mathrm{top}}} d\gamma(\eta)\int_0^{\eta} d\gamma(\eta)\int_{\partial\sigma_t}\frac{\partial\bar{u}}{\partial n_\sigma}d\gamma(\zeta)\\
&\quad=\lim_{d\zeta\to 0}\sum_{d\zeta}\frac{2}{\mathrm{Re}}\int_0^{\eta^{\mathrm{top}}} d\gamma(\eta)\int_{\partial\sigma_t}[\bar{u}(\eta)-\bar{u}(0)]d\gamma(\zeta)\\
&\quad=\frac{2U_bA_\Sigma}{\mathrm{Re}}=T_b,
\end{aligned}
\tag{B2}
$$

$$
\begin{aligned}
&\lim_{d\zeta\to 0}\sum_{d\zeta}\int_0^{\eta^{\mathrm{top}}} d\gamma(\eta)\int_0^{\eta} d\gamma(\eta)\int_{\sigma}\int(-2F'')dydz\\
&\quad=\int_{\zeta_1}^{\zeta_2} d\gamma(\zeta)\int_0^{\eta^{\mathrm{top}}} d\gamma(\eta)\int_0^{\eta} d\gamma(\eta)\int_0^{\eta}(-2F'')d\gamma(\eta)\\
&\quad=\int_{\zeta_1}^{\zeta_2}\int_0^{\eta^{\mathrm{top}}}\frac{1}{2}[\gamma(\eta^{\mathrm{top}})-\gamma(\eta)]^2(-2F'')d\gamma(\zeta)d\gamma(\eta)\\
&\quad=\int_{\zeta_1}^{\zeta_2}\int_0^{\eta^{\mathrm{top}}}[\gamma(\eta^{\mathrm{top}})-\gamma(\eta)]^2\\
&\qquad\times\left(-I''_x-\frac{\partial P''}{\partial x}-\frac{\partial u''}{\partial t}\right)d\gamma(\zeta)d\gamma(\eta)=\mathcal{T}_a+\mathcal{T}_p+\mathcal{T}_{\mathrm{tr}},
\end{aligned}
\tag{B3}
$$

$$
\begin{aligned}
&\lim_{d\zeta\to 0}\sum_{d\zeta}\int_0^{\eta^{\mathrm{top}}} d\gamma(\eta)\int_0^{\eta} d\gamma(\eta)\int_{\partial\sigma_t}(-2\overline{u'v'_{n_\sigma}})d\gamma(\zeta)\\
&\quad=\int_{\zeta_1}^{\zeta_2}\int_0^{\eta^{\mathrm{top}}}[\gamma(\eta^{\mathrm{top}})-\gamma(\eta)](-2\overline{u'v'_{\eta}})d\gamma(\zeta)d\gamma(\eta)\\
&\quad=\mathcal{T}_t.
\end{aligned}
\tag{B4}
$$

Integration by parts was used to transform multiple integrations over $\eta$ to a single integration in the derivation of Eqs. (B1), (B3), and (B4). $U_b$ in Eq. (B2) is the (nondimensional) bulk velocity.

[1] M. Gad-El-Hak, *Flow Control* (Cambridge University Press, Cambridge, England, 2000).

[2] S. K. Robinson, "Coherent motions in the turbulent boundary layer," Annu. Rev. Fluid Mech. **23**, 601 (1991).

[3] K.-S. Choi, "Near-wall structure of a turbulent boundary layer with riblets," J. Fluid Mech. **208**, 417 (1989).

[4] H. Choi, P. Moin, and J. Kim, "Active turbulence control for drag reduction in wall-bounded flows," J. Fluid Mech. **262**, 75 (1994).

[5] H. Rebbeck and K.-S. Choi, "A wind-tunnel experiment on real-time opposition control of turbulence," Phys. Fluids **18**, 035103 (2006).

[6] M. J. Walsh, in *Viscous Drag Reduction in Boundary Layers*, edited by D. M. Bushnell and J. N. Heffner (AIAA, Washington, DC, 1990).

[7] D. W. Bechert, M. Bruse, W. Hage, J. G. T. Van Der Hoeven, and G. Hoppe, "Experiments on drag-reducing surfaces and their optimization with an adjustable geometry," J. Fluid Mech. **338**, 59 (1997).

[8] A. Ferrante and S. Elghobashi, "On the physical mechanisms of drag reduction in a spatially developing turbulent boundary layer laden with microbubbles," J. Fluid Mech. **503**, 345 (2004).

[9] F. Laadhari, L. Skandaji, and R. Morel, "Turbulence reduction in a boundary layer by a local spanwise oscillating surface," Phys. Fluids **6**, 3218 (1994).

[10] K.-S. Choi, "Near-wall structure of turbulent boundary layer with spanwise-wall oscillation," Phys. Fluids **14**, 2530 (2002).

[11] K. Fukagata, K. Iwamoto, and N. Kasagi, "Contribution of Reynolds stress distribution to the skin friction in wall-bounded flows," Phys. Fluids **14**, L73 (2002).

[12] K. Iwamoto, K. Fukagata, N. Kasagi, and Y. Suzuki, "Friction drag reduction achievable by near-wall turbulence manipulation at high Reynolds numbers," Phys. Fluids **17**, 011702 (2005).

[13] K. Fukagata, N. Kasagi, and P. Koumoutsakos, "A theoretical prediction of friction drag reduction in turbulent flow by superhydrophobic surfaces," Phys. Fluids **18**, 051703 (2006).

[14] T. Gomez, V. Flutet, and P. Sagaut, "Contribution of Reynolds stress distribution to the skin friction in compressible turbulent channel flows," Phys. Rev. E **79**, 035301 (2009).

[15] M. Sbragaglia and K. Sugiyama, "Boundary induced nonlinearities at small Reynolds numbers," Physica D **228**, 140 (2007).

[16] J. Lumley and P. Blossey, "Control of turbulence," Annu. Rev. Fluid Mech. **30**, 311 (1998).

[17] Y. Charron and E. Lepesan, France Patent No. 2899,945 (2007).

[18] Y. Peet, P. Sagaut, and Y. Charron, "Pressure loss reduction in hydrogen pipelines by surface restructuring," Int. J. Hydrogen Energy **34**, 8964 (2009).

[19] D. W. Bechert and M. Bartenwerfer, "The viscous flow on surfaces with longitudinal ribs," J. Fluid Mech. **206**, 105 (1989).

[20] H. Choi, P. Moin, and J. Kim, "Direct numerical simulation of turbulent flow over riblets," J. Fluid Mech. **255**, 503 (1993).

[21] J. Jiménez and P. Moin, "The minimal flow unit in near-wall turbulence," J. Fluid Mech. **225**, 213 (1991).

[22] E. R. Van Driest, "Turbulent boundary layer in compressible fluids," J. Aeronaut. Sci. **18**, 145 (1951).

[23] F. Archambeau, N. Méchitoua, and M. Sakiz, "CODE_SATURNE: A finite volume code for the computation of turbulent incompressible flows—industrial applications," Int. J. Fin. **1**, 1 (2004).

[24] J. Smagorinsky, "General circulation experiments with the primitive equations," Mon. Weather Rev. **91**, 99 (1963).

[25] Y. Peet, P. Sagaut, and Y. Charron, 38th AIAA Fluid Dynamics Conference and Exhibit, Seattle, WA, 23–26 June 2008.

[26] Y. Peet, P. Sagaut, and Y. Charron, 5th IASME/WSEAS International Conference on Fluid Mechanics and Aerodynamics, Vouliagmeni, Greece, 25–27 August 2007.

[27] H. Abe, H. Kawamura, and Y. Matsu, "Direct numerical simulation of a fully developed turbulent channel flow with respect to Reynolds number dependence," ASME J. Fluids Eng. **123**, 382 (2001).

[28] H. Choi, P. Moin, and J. Kim, "On the effect of riblets in fully developed laminar channel flows," Phys. Fluids A **3**, 1892 (1991).

[29] D. Goldstein, R. Handler, and L. Sirovich, "Direct numerical simulation of turbulent flow over modeled riblet covered surface," J. Fluid Mech. **302**, 333 (1995).

[30] W. J. Jung, N. Mangiavacchi, and R. Akhavan, "Suppression of turbulence in wall bounded flows by high-frequency spanwise oscillations," Phys. Fluids A **4**, 1605 (1992).

[31] A. Baron and M. Quadrio, "Turbulent drag reduction by spanwise wall oscillations," Appl. Sci. Res. **55**, 311 (1996).

[32] P.-A. Krogstad, J. H. Kaspersen, and S. Rimestad, "Convection velocities in a turbulent boundary layer," Phys. Fluids **10**, 949 (1998).